PARAMETRIC FREQUENCY COMB GENERATION IN VISIBLE AND MID-INFRARED WAVELENGTHS WITH INTEGRATED SILICON NITRIDE RING RESONATORS

A Dissertation

Presented to the Faculty of the Graduate School

of Cornell University

in Partial Fulfillment of the Requirements for the Degree of

Doctor of Philosophy

by

Kevin James Luke

February 2016

© 2016 Kevin James Luke

ALL RIGHTS RESERVED

PARAMETRIC FREQUENCY COMB GENERATION IN VISIBLE AND MID-INFRARED WAVELENGTHS WITH INTEGRATED SILICON NITRIDE RING RESONATORS

Kevin James Luke, Ph.D.

Cornell University 2016

The field of silicon photonics allows manipulation of light at the chip-scale. Although the field has its roots in the telecommunications industry and its potential for low-power, high-bandwidth data transmission, the field has since expanded to a myriad of new applications, such as nonlinear optics, quantum optics, opto-mechanics, and opto-genetics. Nonlinear optics, in particular, has advantages in chip-scale devices that are not available in larger free-space or fiber-based systems. Because light can be confined to extremely small volumes in on-chip devices, nonlinear effects can be strongly enhanced. In this dissertation, we will focus on the nonlinear process of optical frequency comb generation, engineered for wavelengths outside of the standard telecom regime.

In Chapter 1, we will begin with overall motivation for the field of silicon photonics. We will introduce basic theory of the origin of nonlinearity and its role in the frequency comb generation process. The ring resonator, the workhorse of integrated nonlinear optics, will also be introduced.

Chapter 2 explains in detail the device fabrication. First a generic process overview applicable to fabrication of most photonic devices will be presented. A more detailed baseline process will be introduced, followed by the major processing improvements that were necessary for the chapters following. Finally, specific optimizations of the etch process which enabled work in Chapter 5 will

be detailed.

In Chapter 3, we overcome traditional film thickness limitations in order to improve device quality. We employ a trench technique to isolate cracks from the device region, and as a result we improve the quality factor of devices. Ultimately, we measure record high quality factor devices.

Chapter 4 discusses comb generation in the mid-infrared (MIR) wavelength range. We overcome challenges in dispersion engineering by employing the crack isolation trenches in Chapter 3 to grow required film thicknesses, and we optically characterize materials in the MIR wavelength range. We also improve MIR losses by annealing films periodically throughout the film growth. Ultimately, we demonstrate MIR comb generation.

In Chapter 5, we pursue comb generation in visible wavelengths. After initial demonstrations, we present a comb with low phase-noise and a comb with a smooth envelope. We apply a finely spaced comb for a biomedical imaging technique (OCT) to generate fully three dimensional images. Finally, a route to comb generation for even lower wavelengths is presented.

In the final chapter, we discuss future work. This includes improving the quality factors in the telecom wavelengths, generating deeper into the MIR using suspended structures, and stabilizing visible combs by locking to atomic lines. Improvements on the initial biomedical imaging work in Chapter 5 are also discussed.

BIOGRAPHICAL SKETCH

Kevin James Luke was born in a small village in India in 1988. Both of his parents grew up on farms, but only 1 year after Kevin's birth, the small family moved to the United States. The family moved around quite a bit in the early years, but eventually settled in a suburb of New Jersey, where the family stayed from 2nd grade onwards. Kevin worked diligently both academically and in his many extracurricular activities, including soccer, tennis, dramas, musicals, and various clubs. Although these efforts were at the expense of a thriving social life and various formative experiences throughout adolescence, he was eventually rewarded for his efforts, graduating at the top of his class and being admitted to Columbia University. During this time, Kevin transformed from the "naive goody two-shoes" character of his high school days into the "awkwardly frustrated and uncomfortable" character of his college years. Thriving academically, Kevin also sought balance by joining the Columbia Bhangra team (an Indian folk dance) and later the breakdance team Raw Elementz. He also enjoyed several excursions into the nightlife of NYC, but ultimately practical concerns (lack of income and insurmountable debt) limited these activities. Practical concerns also led him away from his natural clemency towards Computer Science and Applied Mathematics, to Electrical Engineering (although he still managed to minor in both of the other subjects). After his junior year of undergraduate, Kevin completed a summer internship at Lawrence Livermore National Lab (LLNL) and was inspired by the scientists around him to pursue research. When he arrived back at Columbia, he was fortunate enough to experience research under Professor Keren Bergman's group, in the field of integrated optical systems. After graduating Magna Cum Laude in 2010, his interest in the device side of the research naturally led him to Cornell University, where he pursued

his Ph.D. under the direction of Professor Michal Lipson. Throughout his time at Cornell, Kevin underwent several character transformations, ultimately settling on the "wise beyond his years, yet eternally youthful at heart" character. Kevin has immensely enjoyed his time in Ithaca while being able to work on interesting and relevant problems as a member of the Cornell Nanophotonics Group.

To my two younger brothers, Jonathan and Dylan. You inspire me to contribute to a better tomorrow.

ACKNOWLEDGEMENTS

First of all, I would like to thank my advisor, Professor Michal Lipson. The impact she has had on the field of nanophotonics is profound, as evidenced by her many high impact publications and prestigious awards, but it did not fully occur to me until the end of my Ph.D. When she announced that the lab will be moving to Columbia, I finally realized that she no longer *follows* the field; she *is* the field. Wherever she is, that is where the forefront of nanophotonics research will be. Aside from her clear academic successes, I also admire her for her strong interpersonal skills and general sensitivity to the people around her. Unlike the caricatured slave-driving professors that graduate students often joke about, Michal has a deep and intimate knowledge of the various personalities and needs of the people she works with. I feel privileged that I could absorb some of these qualities from her over the past 5 years. I could not have found a more compatible person to advise me in my graduate studies.

I would also like to acknowledge the other members of my committee: Professors Clifford Pollock and Alexander Gaeta. Cliff has been a quiet inspiration for me, as well as a source of encouragement. Alex has provided me with excellent technical feedback throughout the years, and his sense of the bigger picture and his physical intuition have likewise inspired me.

I would like to thank the funding agencies that have sponsored this research including the National Science Foundation (NSF) through the Integrative Graduate Education and Research Traineeship (IGERT) fellowship, the Cornell Nanofabrication Facility (CNF), the Cornell Center for Nanoscale Science, and the Defense Advanced Research Projects Agency (DARPA).

I am indebted to many individuals associated with the research group, who helped me get started in the very beginning of my time at Cornell. Dr. Michael

Menard was the first person to introduce me to fabrication. Dr. Jacob Levy, my predecessor in Si_3N_4 comb generation, quickly got me up to speed with fabrication, to the point where I was fabricating chips within a few months of his guidance. Dr. Carl Poitras was always there to pick up any of my slack, and he always approached my technical, logistical, or administrative issues with the same poise and calm. Dr. Arthur Nitkowski, Dr. Nicolas Sherwood Droz, and Dr. Kyle Preston guided me through many of my early hiccups and also continued to support my research pursuits through our collaboration with Tornado Medical Systems. Nic, in particular, has demonstrated by example that one can indeed live a life outside of work without the typically stark work-life separation. I thank Dr. Michael Lamont for his patience in teaching me about theoretical fundamentals needed for my research; I owe a large part of my strong technical intuition to him. Also, the long-gone Brazilians, Professor Lucas Gabrielli and Professor Gustavo Wiederhecker, I thank you for your inspiring physics discussions during my time at Cornell, and I hope to meet you again in Brazil sometime in the future (or elsewhere, but preferably Brazil). To my fellow labmates Dr. Lawrence Tzuang, Dr. Austin Griffith, Dr. Yoon Ho Daniel Lee, and Shreyas Shah, who started out with me and have spent the past 5 years struggling alongside me: as fellow batchmates I could not help but feel inspired and encouraged by your many successes. Going forward, I would like to thank the more recent students, Brian Lee, William Ji, Gaurang Bhatt, Ipshita Datta, Moshe Zadka, Brian Stern, and Amin Tadayon, for the pleasure of getting to know you in the short time we have overlapped.

There are many other individuals in the research group I would like to thank. Romy Fain, thank you for being the most interesting individual I have ever met, and I will be in eternal competition to become just as interesting. I also re-

member the “jumping from project to project” phase of research, but it ends eventually, and I wish you the best of luck. Christopher Phare, thank you for your random technical help on anything I ask you about. You are a fountain of knowledge, and it was always extremely comforting knowing that you (almost always) had the answer to one of my questions when even Wikipedia did not. Dr. Mian Zhang, your understanding for the physical relationships between quantities and you concise but insightful ability to communicate that knowledge has always been an inspiration to me, and I seek to understand everything in a similar manner. We have not had as many conversations as I would have like, but whenever we did, I was always surprised by how in-depth our conversations quickly became. Dr. Felippe Barbosa, I have always admired your ability to explain even the most complex concepts (quantum mechanics being one of those) in very simple and intuitive ways. We think very similarly, which I believe is why we have been able to find solutions to many technical problems through our discussions. I hope everything stays “tudo bem” with you, “meu amigo”. And yes, I have a perfect Brazilian accent. Dr. Raphael St-Gelais, thank you for your insights into anything thermal, whether it be about the thermal shifting of my resonance or about something silly like global warming. You are one of the most intelligent people I know, both in book smarts and street smarts, but also quite humble in your own way. Of course, I will never tell you all of this in person, because your accent already sounds arrogant enough as it is. Finally, I would like to thank Dr. Jaime Cardenas. Without you, there would be no group. Michal once said that devices turn out as good as the group that makes them, and you are the reason our devices are the leading devices in the field. Your expansive knowledge of fabrication has directly led us to our current level of success. Yet, despite your extensive knowledge, I admire your strong passion

for teaching and care for the students' experiences. Even if you know the answer, you recognize when to allow students to think for themselves and try out new approaches for themselves. Even though you eventually were asking *me* questions about the Si_3N_4 process, you had a huge role in helping me develop the process. I wish you all the luck in your new role at Columbia.

I would like to thank a few members of the group in particular for their impact on my personal experience in Ithaca. The first of them is Steven Miller, my fellow Si_3N_4 guy. It has been extremely comforting to have another capable dedicated Si_3N_4 fabricator, especially in the beginning when I was alone in a world of silicon. I know that I can rely on you for anything in research, be it unloading a furnace early morning, working through some tricky nonlinear equations, discussing how we would expect a hypothetical system to behave, or advising me on the best way to approach my experiments. In my personal life, you have been a good friend from the start, and you have taught me indirectly about alternative ways of thinking. You also play a mean jazz trumpet solo. For a classically trained guy, you've got some bad chops. Next is Avik Dutt, who I thank for keeping me sane by engaging me on interesting theoretical topics. In a lab full of practical people, you have helped me stay imaginative by exploring my logistically impractical puzzles. As another one of the dwindling night people, you have kept things fresh for me in the otherwise bleak hours of darkness. But also technically, you have been someone I can always double check my logic with, and you are one of the few people who I trust absolutely in doing so. I admire the way you calmly approach new problems and very quickly come to a sense of what the fundamental issue is, or at the very least find a clear pathway to investigating the problem. Finally, Aseema Mohanty, you are the best friend I have ever had. In our time at Cornell, you have helped me grow as a researcher

and even more so as a person. I respect your passion for your research and your pure love for the beauty found in interesting problems. Your patience and understanding has given me the support I needed during the many, many times of struggle. You struggled a lot yourself with your initial project, but now that you have hit your stride, I am excited to see what kind of researcher you will become. You often applaud me for my gift with words, but this is one case in which words cannot fully capture the impact you have had on my life and what your friendship means to me.

Lastly, I would like to thank my family and friends for their support over the past 5 years. My close friends in Ithaca, Shreesha Srinath, Dax Howard, and Suren Jayasuriya, you have helped me find balance in my graduate life and have helped quell my visceral need for intellectual stimulation. And to many of my other friends from Ithaca, particularly Ved Gund, Levon Atoyan, Tayyar Rzayev, Phil Gordon, and Uchita Vaid, you have shaped my experience in Ithaca. Finally, I thank my family for their continued and unconditional support, and for setting me up for the opportunities that eventually led me to where I am now. I fully acknowledge that I did nothing completely on my own; I stand on the shoulders of giants. That applies to everyone I have acknowledged, and the many others I am failing to acknowledge properly in this manuscript. Everything I have accomplished and will accomplish is in some way connected back to you.

TABLE OF CONTENTS

Biographical Sketch . . . iii
Dedication . . . v
Acknowledgements . . . vi
Table of Contents . . . xi
List of Figures . . . xiv

1 Introduction **1**
1.1 Basic Theory . . . 2

2 Device Fabrication Improvement **5**
2.1 Process Overview . . . 5
2.1.1 Handle Wafer . . . 5
2.1.2 Film Stack Creation . . . 5
2.1.3 Patterning . . . 6
2.1.4 Etching . . . 7
2.1.5 Resist Stripping . . . 8
2.1.6 Cladding . . . 9
2.2 Baseline Process . . . 9
2.2.1 Starting Wafer . . . 10
2.2.2 Grow BOX . . . 10
2.2.3 Deposit Si_3N_4 . . . 10
2.2.4 Spin e-Beam Resist . . . 11
2.2.5 Spin Anti-Charging Layer . . . 11
2.2.6 Draw CAD . . . 12
2.2.7 Expose e-Beam Resist . . . 12
2.2.8 Develop e-Beam Resist . . . 14
2.2.9 Descum e-Beam Resist . . . 14
2.2.10 Hard Bake e-Beam Resist . . . 15
2.2.11 Etch Si_3N_4 . . . 15
2.2.12 Etch Backside Si_3N_4 . . . 16
2.2.13 Strip e-Beam Resist . . . 16
2.2.14 Geometry Measurement . . . 17
2.2.15 Anneal Si_3N_4 . . . 17
2.2.16 Clad with thin Oxide . . . 18
2.2.17 Clad with thick Oxide . . . 19
2.2.18 Define Facet . . . 19
2.3 Process Improvements . . . 20
2.3.1 Grow BOX: Long Dry Oxidation . . . 20
2.3.2 Deposit Si_3N_4: Trench Definition, Argon Anneal . . . 21
2.3.3 Spin Anti-Charging Layer: Removed . . . 22
2.3.4 Draw CAD: Rounder Polygons, Single Field Devices . . . 22
2.3.5 Expose e-Beam Resist: Proximity Error Correction . . . 25

2.3.6 Descum e-Beam Resist: Removed 27
2.3.7 Hard Bake e-Beam Resist: No Reflow 27
2.3.8 Etch Si_3N_4: Reduced Oxygen 29
2.3.9 Etch Backside Si_3N_4: using Recessed Wafer (Optional) . . 29
2.3.10 Strip e-Beam Resist: Chemical Stripping 32
2.3.11 Geometry Measurement: Measure Waveguide Profile . . . 33
2.3.12 Anneal Si_3N_4: Argon Anneal 35
2.3.13 Define Facet: Etched Facets 36
2.4 Optimized Etch Process 39
2.4.1 Etch Chemistry Optimization 39
2.4.2 Process Modifications 39

3 Overcoming Stress Limitations for High *Q* **42**
3.1 Introduction 42
3.2 Loss Reduction 43
3.3 Crack Isolation Trenches 44
3.4 High *Q* Measurement 47
3.5 Summary 49

4 Frequency Comb Generation in the Mid-Infrared **50**
4.1 Introduction 50
4.2 Dispersion Engineering 50
4.3 Optical Characterization of Si_3N_4 51
4.4 Growing Thick Si_3N_4 Films 52
4.5 Improving Absorption Loss 54
4.5.1 Absorption Loss Estimation 55
4.5.2 Cladding Anneal 56
4.5.3 Mid-Deposition Anneal 57
4.6 Comb Generation 59
4.7 Summary 62

5 Frequency Comb Generation near Visible Wavelengths **63**
5.1 Introduction 63
5.2 Dispersion and Comb Simulation 64
5.3 Initial Experimental Comb 65
5.4 Low Phase Noise Comb 67
5.5 Smooth Envelope Comb 70
5.6 Optical Coherence Tomography (OCT) Measurement 75
5.7 Pushing Further Towards Visible Combs 79
5.8 Summary 85

6 Summary and Future Work **88**
6.1 Higher Q with Thicker Si_3N_4 88
6.2 MIR Combs with suspended Si_3N_4 88
6.3 Locking to Atomic Lines 89
6.4 High Resolution OCT Imaging 90

Bibliography **91**

LIST OF FIGURES

1.1 Schematic of an ideal parabolic potential, versus the actual potential of a real material. The distortion gives rise to optical nonlinearity. Image used from [1]. 3

2.1 Overview of the basic process used to create most nanophotonic structures. Each image is a schematic of the cross section after performing the processing listed in each step. 6
2.2 SEM of the coupling gap between a straight bus waveguide and a 46 µm ring resonator. Note the significant distortion of the rounded ring section on the right; we can see the curved section has been approximated by three different line segments (outlined in red). This distortion can only be seen on the SEM; when zoomed out far enough, these segments are small enough to appear perfectly circular. 24
2.3 SEM of a line that suffered stitching error. Instead of a single continuous line, we see two lines, with the line on the right shifted down and left from its intended position. 25
2.4 Screenshots of the results of PEC using BEAMER. A few ring resonators are shown in (a), scale bar of relative dose from 1.348 to 1.612 in (b), and an expanded image a coupling region in (c). Note that there is significant dose correction from the case of an isolated waveguide (green) in the nanotaper region (red) and the coupling region (blue) because of the change in the density of the pattern. Also note that the devices are placed within a single e-Beam write field (black), as explained in Section 2.3.4 26
2.5 AFM scans of the resist after hard bake with (a) the previous process at 135°C and (b) the improved process at 115°C. The rounded shape in (a) is a characteristic signature of reflow, whereas the sharp vertical right edge in (b) signifies that the resist is no longer reflowing. Note that when there are sharp edges in the topology, we expect an asymmetric scan. This is an artifact of the AFM measurement, and is discussed further in Section 2.3.11 28
2.6 Schematic of the process used to prepare the device wafer for the backside etch using a recessed wafer. The device wafer is placed upside down on the recessed wafer, with photoresist (red) used to seal the wafers together. The gap between the device region and the recessed wafer prevents physical damage to the devices. 33

2.7 (a) Schematic of the AFM measurement and (b) actual data from an AFM measurement on a waveguide cross section. The AFM tip (grey) taps the surface as it scans left to right (denoted by red arrow and dotted red trace) or right to left (blue arrow and dotted blue trace). Note that for both traces, the left side of the waveguide cannot be resolved because of the angle of the AFM tip; as the tip scans, the right side of the tip eventually contacts the corner of the waveguide and the tip cannot access closer to the base of the waveguide. However, on the right side of the waveguide, the blue direction can resolve the sidewall, whereas the red direction cannot because the tip cannot lower itself fast enough to keep up with the steep sidewall. For the data in (b), we only record the blue trace. 35
2.8 Schematic of the etched facet process flow (showing side view of nanotaper). First we coat and pattern photoresist, leaving a few μm gap between the patterned facet edge and the tip of the nanotaper. Then we etch into the cladding and bottom oxides, and then the silicon substrate to allow close access for lensed fibers or focused free-space beams. After stripping the remaining photoresist, we can dice to singulate the chips (not shown). 37

3.1 Transverse electric (TE) mode simulations at 1550 nm wavelength for the (a) 400 nm x 1800 nm and (b) 910 nm x 1800 nm waveguides with 71% and 93% modal confinement, respectively. Less of the optical field interacts with the waveguide boundaries for the taller waveguide (b). 43
3.2 Microscope images in the dark field showing crack propagation terminating at a trench created with a diamond scribe. The film to the left of these trenches is crack free. 45
3.3 Scanning electron microscope (SEM) image of the resonator. . . . 46
3.4 (a) Transmission spectrum with the finely scanned resonance outlined in red. (b) Resonance with 36 MHz linewidth corresponding to an intrinsic Q of 7 million. 48

4.1 Refractive index n and extinction coefficient k for the wavelength range 1.4-32 μm. Extrapolation from NIR Sellmeier equations (blue) shows no influence from the MIR absorption peak, as expected. However, the measured absorption peak near 10 μm (red) strongly influences the measured refractive index (green), and the fitted Sellmeier equation (dotted green) agrees well with the measurement in the spectral range between 1.4 and 4 μm (see inset). As shown in the inset, at shorter wavelengths, even as far as the telecom wavelength range, the refractive index is significantly influenced by the MIR absorption peak. 53

4.2 Resonance spectrum measured around λ_0=2.6 μm for devices fabricated with single anneal during Si3N4 film deposition but without post-fabrication annealing (blue), with post-fabrication annealing (green), and multiple annealing (red) during Si3N4 film deposition. For devices with cross section 910 nm tall by 2.4 m wide, the Q improves from Q=55,000 with single anneal during deposition (blue) to Q=200,000 after a long post-fabrication anneal for 13 hours at 1100C (green). The resonance extinction increases as expected, since reduction in losses transitions the resonance from under-coupled to critically-coupled regime. With multiple annealing during film deposition (red, inset) of devices with cross section 950 nm tall by 2.7 m wide (the devices used for comb generation in this work), the Q improves to Q=1,000,000. 57
4.3 (a) Schematic of the deposition-anneal cycling process. After the thermal oxide under-cladding and trenches are formed, we deposit silicon nitride via LPCVD and then anneal at 1200°C. We deposit another silicon nitride layer, anneal, and then deposit the final layer. The final layer is annealed before cladding the devices. (b) Scanning electron microscope image of fabricated ring resonator of radius 230 μm and gap of 860 nm. We implement an adiabatic coupling region as in [2] to minimize excitation of higher order modes. (c) Schematic of resonator cross section of 950 nm tall by 2.7 m wide. 60
4.4 (a) Experimentally generated frequency comb spanning 2.3 to 3.5 μm. The different noise floors are due to optical filtering necessary to overcome the limited dynamic range of the FTIR. Inset shows the the dispersive wave beginning to form, as predicted by simulations in (b). 61

5.1 Simulations of (a) resonator dispersion, (b) frequency domain of the comb, and (c) time domain of the comb. At high enough pump power or quality factor, we expect to see single-pulse modelocking occur in the resonator. 64
5.2 Schematic of experimental setup. The broad red beam denotes free-space optics, whereas the narrow red lines denote fiber. YDFA: ytterbium-doped fiber amplifier, Pol: polarizer, $\lambda/2$: half waveplate, BPF: 10 nm bandpass filter centered at 1064 nm, PD: photodiode, OSA: optical spectrum analyzer. 66
5.3 (a) SEM of 46 μm ring resonator used to generate frequency comb. Coupling gap is 380 nm, and the ring resonator cross section (b) is 690 nm tall by 1400 nm wide. 67

5.4 (a) Frequency comb simulation , (b) experimentally measured comb, and (c) inset of the comb lines generated at the short wavelength edge of the comb. The predicted comb bandwidth agrees well with that of the measured comb. 68
5.5 Schematic of experimental setup. The broad red beam denotes free-space optics, whereas the narrow red lines denote fiber. The NF allows for monitoring of the reflected pump power and also increases the dynamic range of the OSA. With fiber splitters, we can also simultaneously monitor (not including the pump) the comb power, the optical spectrum, and the electrical noise spectrum. YDFA: ytterbium-doped fiber amplifier, Pol: polarizer, BPF: 10 nm bandpass filter centered at 1064 nm, $\lambda/2$: half waveplate, NF: 50 nm notch filter centered at 1064 nm, PD: photodiode, FPD: fast photodiode (maximum bandwidth of 350 MHz), OSA: optical spectrum analyzer. 70
5.6 (a) Oscilloscope traces of pump power (teal) and comb power (red) while tuning the pump wavelength through resonance. Note the sudden step transition for both pump power and comb power near the end of the scan. This step in the resonance scan is consistent with previous observations of low-noise combs. Measuring the optical spectrum before (b) and after (c) this step reveals a change in the comb structure, also consistent with a comb state change seen in previous observations. We also monitor the comb on a fast photodiode and record the RF noise spectra (d) before and after this transition. The observed drop in the RF noise is also consistent with low-noise observations. The optical spectrum in (e) is an high resolution scan of the comb after the transition, and we verify that the comb remains fully filled in after the transition. 71
5.7 Experimentally generated frequency comb with smooth comb envelope. The region around the 1060 nm pump is filtered by a notch filter in order to increase the dynamic range of the OSA. Note the smoother spectrum, particularly around the 850 nm range, which is suitable for OCT applications. 74
5.8 Experimentally generated frequency comb with a ring resonator of radius 287 μm, corresponding to 80 GHz comb spacing. The individual comb lines are not resolved because the comb spacing is smaller than the spectrometer resolution. The inset shows a high resolution scan over the range relevant for the OCT measurement. Generation from 800 - 900 nm is ideal, but we successfully obtain images using the generated 850 - 900 nm range. . . . 78

5.9 Simplified experimental setup for spectral domain optical coherence tomography (SD-OCT). A broadband source is split into a reference arm and sample arm, and then recombined and sent to a spectral detector. By varying the reference arm and analyzing the spectrum, we extract axial depth information. The sample arm is usually raster scanned to obtain lateral information, in order to form a full 3D image. Often, the broadband source is spectrally filtered, but for our measurements we replace the broadband source with a frequency comb source. Image is provided by Tornado Spectral Systems. 80
5.10 Result images of OCT measurement of an aspirin pill using the on-chip frequency comb as the light source. We can clearly distinguish the 'ASPIRIN' text label on the pill. There are a few surfaces that appear above the pill; these are artifacts introduced by non-optimal spectral sampling, and can easily be removed with image post-processing 81
5.11 Simulation of the coupling strength of a directional coupler across wavelength, for various gaps. For each gap, the coupling length has been adjusted to create identical values of coupling at the pump wavelength of 1060 nm. Note that the coupling is a strong function of wavelength, even for the smallest gap value of 100 nm. 83
5.12 CAD of a resonator with MZI coupling region embedded. The heaters (purple) can tune the MZI path length difference (yellow) and the resonator itself (yellow) independently. The area outlined in red can be considered as a single effective coupling region. 84
5.13 Simulation of the embedded MZI coupler for different path length differences using Equation 5.2. In all cases, κ has been set to 0.5, so that the maximum value of κ_{eff} is normalized to 1. For the set of path length differences shown in (a), 0.36 μm (bold green) cancels the coupling dispersion well, and similarly 0.5 μm (bold yellow) in (b). (c) shows that for sufficiently large path length difference, the periodicity changes too quickly; either coupling at the pump wavelength, coupling at the shorter wavelengths, or coupling at the longer wavelengths are significantly blocked. 86

CHAPTER 1

INTRODUCTION

In the past decade, we have seen a tremendous growth in the field of integrated photonics. The field began with the promise to surpass the approaching end of Moore's Law due to the looming bottleneck in data communication with electronics. Silicon photonics is particularly promising because it utilizes CMOS (complementary metal-oxide semiconductor) materials and fabrication techniques. Therefore, silicon photonics has the advantage of leveraging the existing billion dollar infrastructure built around the electronics industry. Silicon photonic devices can in principle be mass produced at low cost, with minimal modification of CMOS fabrication; a silicon photonics device has the potential to go from research to industrial product within a few years.

Although the field of silicon photonics was founded in telecommunications, it has since then expanded well beyond its initial conception, and now has applications to a plethora of fields, including gas sensing, biomedical imaging, nonlinear optics, opto-mechanics, and quantum optics to name a few. In this work, we will focus on nonlinear optics applications of silicon photonics. For nonlinear optical processes to occur, we require high optical intensities; the more photons packed in a smaller area, the more influence they will have on each other. Integrated photonics has a fundamental advantage in this regard. Many of the CMOS materials exhibit high nonlinearity, and integrated waveguides naturally confine light to very small (usually sub-wavelength) volumes. What was previously only achievable with large, extremely high power lasers, can now be done routinely on-chip with modest power levels. As the field of silicon photonics continues to advance, linking devices of different functionalities (e.g.

laser source, nonlinear device, and detector) together on a single integrated chip can pave the way for complete photonic systems on-chip.

1.1 Basic Theory

Optical nonlinearity arises when a material's response to electric field deviates from the expected linear response. No material is perfect, and although we often model an electron in a perfectly parabolic atomic potential (which corresponds to a perfectly linear response), real materials have a potential that deviates from this (see Figure 1.1). This distortion of the atomic potential gives rise to higher order response terms (the nonlinear response), which result in optical nonlinearity. These nonlinear response terms can generate new frequencies of light, and the efficiency of this conversion depends on the strength of the nonlinear interaction as well as energy and momentum conservation requirements.

The primary optical nonlinearity we will discuss in this dissertation arises from the material's third order, or $\chi^{(3)}$, nonlinearity. This nonlinearity gives rise to the process of four-wave mixing (FWM), in which two photons interact to create two photons of new frequencies (called the signal and idler frequencies). The efficiency of this process depends on several parameters, but in the case where the parametric gain of this process overcomes the total optical loss for a particular optical frequency, optical parametric oscillation (OPO) occurs, in which signal and idler photons are generated spontaneously. The threshold of this process goes as

$$P_{th} \approx 1.54 \left(\frac{\pi}{2}\right) \frac{Q_C}{2Q_L} \cdot \frac{n^2 V}{n_2 \lambda_P Q_L^2} \tag{1.1}$$

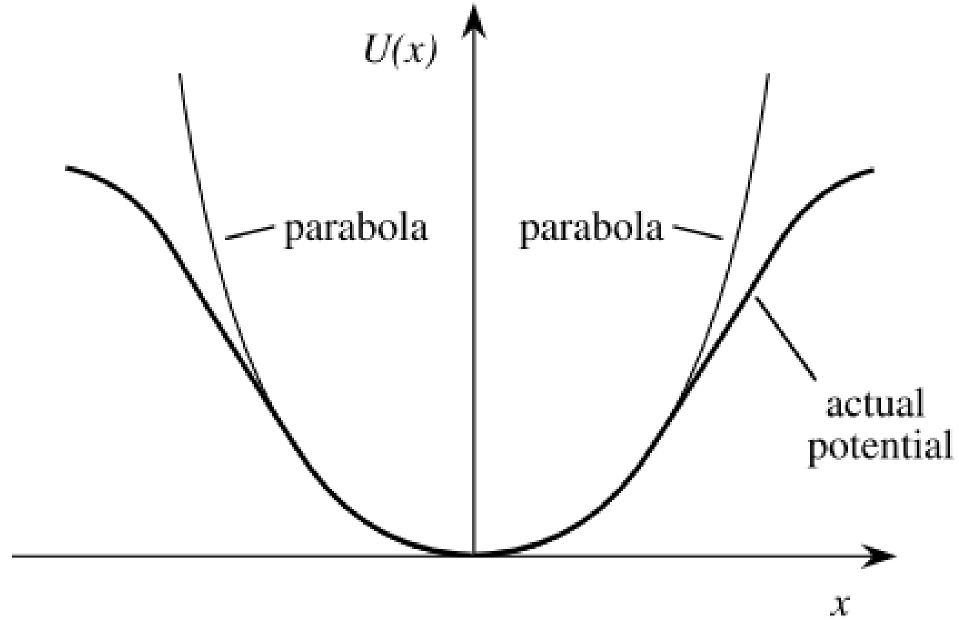

Figure 1.1: Schematic of an ideal parabolic potential, versus the actual potential of a real material. The distortion gives rise to optical nonlinearity. Image used from [1].

where P_{th} is the threshold optical power, Q_C is the coupling quality factor, Q_L is the loaded quality factor, n is the refractive index of the optical mode, V is the mode volume, n_2 is the Kerr nonlinearity of the material, and λ_P is the pump wavelength. If the signal and idler become strong enough, the FWM process can cascade to generate more lines. Once all of the lines are equally spaces in frequency, it is termed a frequency comb.

The workhorse of integrated nonlinear optics are ring resonators. These resonators allow light to build up power internally, creating very high circulating intensities that can be used to enhance nonlinear interactions. The integrated ring resonator is an attractive platform for nonlinear optics because it allows nonlinear interactions to occur in a small device footprint with relatively low

power. The degree of power enhancement within the resonator is related primarily to its losses, which is inversely related to its quality factor (Q). The higher the Q, the higher the power enhancement within the resonator, and the lower the required input power for efficient nonlinear interaction.

CHAPTER 2

DEVICE FABRICATION IMPROVEMENT

2.1 Process Overview

In order to understand the overall process, we will present a very simplified overview of device fabrication. Most nanophotonic processing uses variations of the basic process shown in Fig. 2.1. Note that there are many details that have been hidden between each of these steps, and each of these steps contain many nuances within them that have significant impacts on device quality.

2.1.1 Handle Wafer

We begin with the handle wafer on which we will perform our processing. The most common handle wafers used are silicon and fused silica, typically in 4 inch diameter size because of compatibility with cleanroom facility equipment. However, other substrates are also available.

2.1.2 Film Stack Creation

We then create our film stack on the handle wafer. The materials in this stack will comprise the core and undercladding of the optical waveguide (in some cases the handle wafer material may be used as the undercladding), and the thickness of this core layer will determine the height of the waveguide. In our case, Si_3N_4 will form the core, and SiO_2 will form the undercladding. One

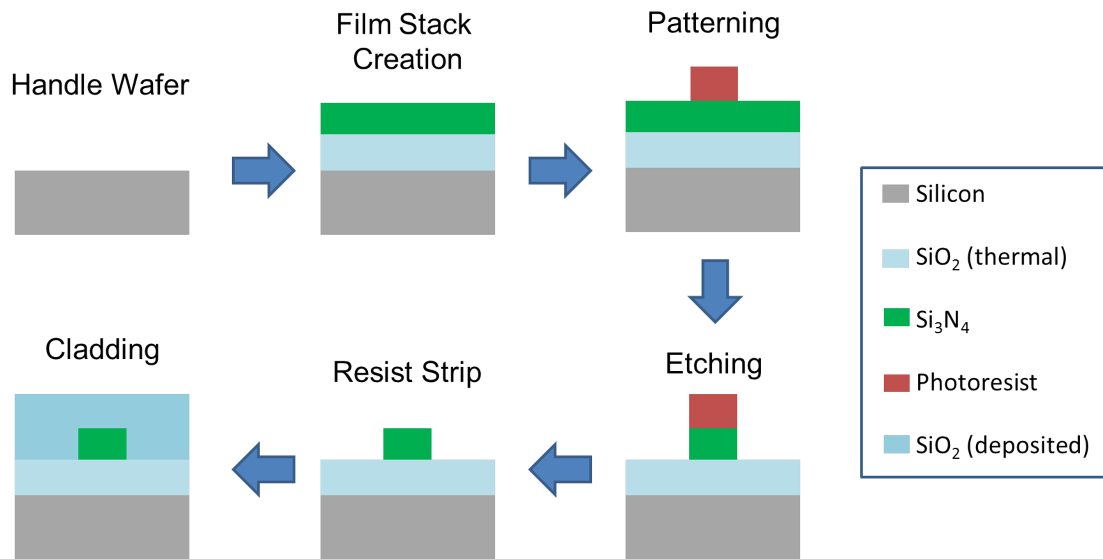

Figure 2.1: Overview of the basic process used to create most nanophotonic structures. Each image is a schematic of the cross section after performing the processing listed in each step.

can deposit more complicated film stacks and use the same processing to create waveguides with interesting properties [3, 4]. The advantage of defining complex structures with film deposition (as opposed to patterning, discussed in the next section), is that film thicknesses can be controlled much more precisely than lithography and etching.

2.1.3 Patterning

We then pattern the wafer. This is done by depositing (usually via spin-coating) a chemical "resist" onto the wafer, which can then have a pattern lithography defined. In photolithography, photoresist is spun onto the wafer, and then a patterned chrome mask is used to expose patterned areas to ultraviolet light. The photoresist is photosensitive, so after applying developer chemicals to the

resist, the patterned areas will wash away (for "positive" resist) or remain intact (for "negative" resist). This will effectively transfer the mask pattern into the resist. Similarly, in e-Beam lithography, e-Beam resist is used instead, and an electron beam is used to expose areas of resist. For the photonic structures we will show, e-Beam lithography is used for patterning, since it is higher resolution and creates much smoother sidewalls compared to photolithography, which results in lower losses.

2.1.4 Etching

Once patterning is complete, the pattern can be transfered into the film stack. There are several methods to accomplish this, but most fall into the categories of either isotropic or anisotropic etching. Isotropic etching can be performed with wet etching, which involves immersion into chemical solutions that selectively dissolve the material to be patterned. Similarly, gas mixtures are used in vapor etching. Because these methods are isotropic, they distort the pattern being transferred into the film. In particular, they reduce the minimum feature size allowable, or they can undesirably etch underneath areas of the film. However, in some cases underetching is desired, for example for released structures that are free-standing.

Anisotropic etching can be done with both dry and wet techniques. Some chemicals, for example KOH, etch a preferred crystal direction. However, anisotropic wet etching still suffers from the other drawbacks of wet etching mentioned above. Anisotropic dry etching, on the other hand, is an anisotropic etch technique that preserves the pattern well, so patterns are transferred into

the film directly vertically, as shown in Fig. 2.1. Dry etching can use physical processes, chemical processes, or a combination of both. Physical dry etching uses particles with high kinetic energy, usually ions accelerated though a strong electric field, to physically bombard and remove material. This technique is analogous to “chiseling” away the material that is not protected by the pattern on top. Chemical dry etching relies on chemical reactions between the gas etchant and the solid material being etched. The product of this reaction is gaseous, which can then diffuse away from the surface. In this way, material is removed as the film is chemically converted into gaseous products. The optical devices presented in this dissertation are fabricated using reactive ion etching (RIE), which combines both physical and chemical processes. RIE uses reactive gas species accelerated in a strong electric field to create a plasma. This plasma physically and chemically etches the unpatterned areas of the film. The high energy plasma also aids in the chemical process, as the high energy collisions dissociate the gases into more reactive species.

2.1.5 Resist Stripping

The resist from the patterning step must be removed before processing can continue. One method to remove resist is to dissolve the resist in chemicals. Acetone and Isopropanol are common chemicals used to strip resist. Another common, but more chemically aggressive, clean uses Hot Piranha (H_2SO_4 and H_2O_2). However, Hot Piranha is a strong oxidizer and may also react with the film, so caution must be used. This can be advantageous in some circumstances, particularly with Si_3N_4, because it may form a thin oxide on the surface. This oxide will be too small to perturb the optical mode of the waveguide, but it may

smoothen the surface slightly, which would reduce losses.

The other method to strip resist is to use an oxygen plasma. This can be done in most RIE etchers or dedicated resist strip tools. This method essentially burns off the resist. However, oxygen plasma may also have unwanted effects, such as altering the stress of Si_3N_4, or roughening the surface slightly.

2.1.6 Cladding

A final cladding layer is deposited on top of the device to protect the structure from the environment. There are a variety of techniques used to deposit the cladding material, but most commonly used is plasma enhanced chemical vapor deposition (PECVD). This is analogous to RIE etching, but in this case the chemical reaction is dominant, and the existing film is not consumed in the process. The gas species within the plasma react to form a solid film on the surface of the wafer. The advantage of PECVD is that the deposition rate can be fast (100 nm/min), but there may be impurities in the material, which can lead to absorption, as seen in Chapter 4. Therefore, cladding is often done with a thinner high quality cladding material first, and then a thick, lower quality cladding material second.

2.2 Baseline Process

Before discussing improvements to the fabrication process, we must first understand the process upon which we will be improving, so that we have a baseline. An overview of the fabrication process is described in this section.

2.2.1 Starting Wafer

We start with a 4 inch silicon wafer. N-doped or P-doped wafers are both usable.

2.2.2 Grow BOX

We grow the thick undercladding buried oxide (BOX) necessary to isolate the optical mode of the waveguide from the silicon wafer. We thermally oxidize the silicon for a long time to grow a thick layer of high quality silicon oxide. We oxidize the wafers at 1200°C in first an O_2 environment, then H_2O, and finally O_2 again. These different atmospheres are needed to achieve both high quality and large thicknesses of silicon oxide, as detailed further in Section 2.3.1.

2.2.3 Deposit Si_3N_4

We deposit the Si_3N_4 film that will comprise the core of the waveguide. We deposit 350 nm of Si_3N_4 using low pressure chemical vapor deposition (LPCVD) at 800°C. This process reacts NH_3 and dichlorosilane (DCS) SiH_2Cl_2 to form Si_3N_4, H_2, and HCl. This is followed by a high temperature anneal to increase the optical quality of the film by driving out defects. We anneal at 1200°C in N_2 atmosphere. Note that this anneal can only be performed on Si_3N_4 films of thicknesses less than $\sim$ 400 nm; otherwise the films crack catastrophically. Methods to overcome this limitation are described in detail in Section 2.3.2. After annealing, Si_3N_4 deposition is repeated using the same deposition process to achieve the final desired film thickness (typically $\sim$ 750 nm).

2.2.4 Spin e-Beam Resist

We spin-coat e-Beam resist onto the wafer, which will later be patterned. The e-Beam resist we use, MichroChem ma-N 2400, is a negative tone resist, i.e. exposed areas will remain after developing the resist whereas unexposed areas will be dissolved away. This particular e-Beam resist has difficulty adhering to substrates, so we begin with surface preparation to promote adhesion to the wafer. We must first ensure that the wafer surface is hydrophilic. One way to do this is to perform an oxygen plasma clean on the wafer, but an easier way is to perform a Hot Piranha (see Section 2.1.5) clean on the wafer. Both of these methods oxidize the surface slightly, which results in a hydrophilic surface. Once the surface is hydrophilic, we can spin-coat Surpass 3000, an adhesion promotion chemical, with water cleaning before and after application. We apply the resist using a syringe with a 0.1 μm or 0.2 μm filter. Finally, we spin-coat ma-N 2400 with appropriate spin speed and dilution to achieve 800 nm of e-Beam resist thickness. We then perform a pre-exposure bake at 90°C to bake out the solvents in the resist. Note that without the previous surface preparation, the ma-N will delaminate from the wafer during the development step (see Section 2.2.8).

2.2.5 Spin Anti-Charging Layer

We spin-coat an anti-charging layer to reduce distortion of the pattern during exposure. The anti-charging layer we use is ESpacer, a commercially available chemical. This chemical is an electrically conductive polymer that prevents charge from accumulating in a concentrated area of the wafer. If charge accu-

mulates, it can be strong enough to deflect the electron beam during exposure, which can significantly distort the pattern (blurring) or lead to misalignment between exposed sections (stitching error). This layer must be applied immediately before exposure (ideally within 1 hour)

2.2.6 Draw CAD

We create a GDS file that contains a layout of the pattern that will be exposed. Note that this step can be done independently at any time prior, but layout must be finished before exposure. This can be done with graphical programs such as L-Edit, or with scripting such as Python coding with Gdspy. We choose to generate CAD layouts using Gdspy, because scripting allows both flexible device design and simple sweeping of critical device parameters. For example, we can write a script that will produce a general ring resonator coupled to a bus waveguide. Then, depending on waveguide dispersion requirements, we can choose the value for the waveguide width for the desired application, and we can also sweep across several devices the critical parameter of the coupling gap between the waveguide and ring resonator.

2.2.7 Expose e-Beam Resist

We expose the resist with an electron beam to define the pattern within the resist. We expose using an electron beam lithography tool, the JEOL JBX9500FS. For exposure we choose a current of 2 nA, a shot pitch of 2 nm, and a dose of 1000 $\mu C/cm^2$. The current is related to the size of the electron beam, and the

shot pitch determines the spacing between individual shots from the electron beam. Together, these parameters affect the roughness of the sidewall in the pattern. Ideally, a small current and shot pitch would be used, but these cannot be too small because of limitations on the write time and clock speed. For smaller values of current, the e-Beam must dwell for a longer time on a given area to deliver the same amount of dose, which can greatly increase the write time for the resist. The clock speed limitation relates to the discretization of the individual shots from the electron beam. These parameters are related by

$$\text{Maximum Clock Speed} = \frac{\text{Current}}{\text{Dose} \times \text{Shot Pitch}}. \tag{2.1}$$

The minimum dwell time for the e-Beam is determined by the maximum frequency of the clock of the JEOL. Since the dwell time for a given dose is related to both the current and the shot pitch, for large current or small shot pitch values, the necessary dwell time can fall below the minimum dwell time allowable.

The dose is carefully chosen to accurately transfer the CAD pattern into the resist. If the resist is overdosed, patterned areas expand and unpatterned areas shrink. This effectively creates wider waveguides and narrower coupling gaps than the parameters specified in the CAD. On the other hand, if the resist is underdosed, the resist does not expose completely, and after developing the resist, the features may not have the full height of the original resist thickness. In practice, this can result in complete consumption of the resist during the etching step, which can expose the top surface of devices to the etch plasma. This roughness induced on the top surface can be significant enough to render devices unusable.

2.2.8 Develop e-Beam Resist

We develop the resist for 90 seconds using an automated Hamatech-Steag Wafer Processor with AZ®726 MIF Developer, which is a dilution of tetramethylammonium hydroxide (TMAH) in water with surfactants. For negative tone e-Beam resist, TMAH will dissolve away areas that have not been exposed.

The develop time is chosen carefully to ensure proper development. If overdeveloped, the patterned features will shrink and open areas will expand. Note that this has the opposite drawbacks of overexposing. If underdeveloped, patterned features may expand slightly, and open areas will not clear completely, leaving a residue of resist in many areas. In practice, this can result in a thin slab in the coupling gap between the waveguide and ring resonator.

2.2.9 Descum e-Beam Resist

We burn off any resist residue that remains after developing the wafer using an oxygen plasma. We use a resist strip tool for 60 seconds with 100 W power used to generate the oxygen plasma. This is a relatively gentle plasma, because we only want to burn off a thin layer of residue, and we want to avoid attacking the Si_3N_4 layer. The purpose of the descum process is to remove any resist residue that may distort the ideal vertical edge of the resist, particularly the characteristic rounded resist remainder at the base of a patterned feature.

2.2.10 Hard Bake e-Beam Resist

We bake the resist at a high temperature to improve its resilience during the etch step. We bake the resist for 5 minutes at 135°C on a hot plate. The high temperature allows the resist to harden so that when it is exposed to the etch plasma, less of the resist will be etched away, effectively improving the selectivity of the etch.

2.2.11 Etch Si_3N_4

We etch the Si_3N_4 film to transfer the resist pattern into the film. We use a CHF_3/O_2 chemistry on an inductively coupled plasma (ICP)-RIE etcher. We first clean the etching chamber for 10 minutes with an oxygen plasma, and then etch the sample for a maximum of 5 minutes. During etching, we flow 52 sccm of CHF_3 and 4 sccm of O_2.

The O_2 is increased from the default value of 2 sccm in order to minimize polymerization of the e-Beam resist. The additional oxygen effectively "burns" any polymer that is formed during etching, before the polymer can be deposited onto the wafer. This is important because the e-Beam resist we use, ma-N 2400, is notorious for polymerization. However, increasing the oxygen also increases the etch rate of the resist itself, which decreases the etch selectivity.

2.2.12 Etch Backside Si_3N_4

We also etch the Si_3N_4 film on the backside of the wafer. This is a precautionary measure to balance the film stress between the frontside and backside of the wafer, so that the wafer does not crack during the final anneal step. As in the frontside etch, we first clean the etching chamber for 10 minutes, and then etch the backside with the same recipe as above for a maximum of 5 minutes.

After etching for 5 minutes, we repeat this cycle of cleaning and etching on the frontside until the desired etch depth is achieved.

2.2.13 Strip e-Beam Resist

We remove the remaining e-Beam resist using an oxygen plasma. At this point, most of the resist will have been consumed during the etch step, but we must be careful to remove any remaining resist because it will be in immediate proximity to the optical mode of the waveguide. Unfortunately, the e-Beam resist ma-N 2400 is notorious for being difficult to remove. Whereas most photoresists can be removed by soaking in solvents, ma-N requires an oxygen plasma to remove it. This can be done in any resist strip tool, although tools that have stricter material restrictions or are generally "cleaner" are preferred, because any impurities that are deposited at this point will be in close proximity to the optical mode of the waveguide. Note that after this step, the devices are completely exposed to the environment, so until cladding is completed the remainder of the fabrication process should be performed in as minimal time as possible to prevent contamination of the devices. However, this is mostly a precautionary measure, since significant environmental contamination has not been conclusively shown

to affect device quality.

2.2.14 Geometry Measurement

At this point, we measure the final geometries of the devices, either with the scanning electron microscope (SEM) or the atomic force microscope (AFM). Measurements cannot be easily made after this point in the process because the cladding will interfere with both SEM and AFM measurements. The silicon oxide cladding, because it is a dielectric, allows charge to accumulate at the surface, which distorts the electron beam of the SEM, preventing accurate measurement. The cladding also physically blocks the AFM probe from accessing the waveguide surface. However, in this baseline process only SEM measurements are taken; AFM measurements are explored further in Section 2.3.11.

Typical measurements include measuring the nanotaper width, waveguide width, waveguide sidewall angle, and coupling gap. These parameters may differ from the parameters specified in the CAD layout because of non-optimal exposure, develop time, or etch chemistry. It is important to measure these parameters precisely because they can have profound impacts on the dispersion properties and coupling conditions of the resonator.

2.2.15 Anneal Si_3N_4

We anneal the wafer at high temperature in order to improve the optical quality of the top layer of the Si_3N_4 film. Recall that during deposition of the film (see Section 2.2.3), the first deposited layer of Si_3N_4 is annealed, but the second layer

is not annealed. Because most of the film has been etched away at this point, we can now safely anneal the second layer of the film without cracking occuring. We perform an identical anneal to the anneal detailed in Section 2.2.3.

2.2.16 Clad with thin Oxide

We deposit a thin high quality oxide to provide initial cladding for the devices. We use LPCVD high temperature oxide (HTO) because of its high material quality and conformal deposition. Because the undercladding is formed using thermal oxidation, the bottom oxide is of extremely high quality. Therefore, in order to create a symmetric structure, we require a high quality oxide for the top oxide. Although we cannot thermally oxidize a top oxide, HTO is of sufficiently high quality. Unfortunately, the deposition rate of HTO is extremely slow, on the order of 1 nm/min, so depositing a thick cladding with HTO would take a preclusively long time. Therefore, we compromise by depositing between 300 and 500 nm of HTO, so that most of the optical mode of the waveguide will interact with the HTO cladding, as opposed to the PECVD cladding of the next step.

HTO also deposits conformally to the surface, allowing the oxide cladding to deposit along steep edges and within small gaps. This is important for low loss devices, because nonconformal deposition processes can leave voids in the film, which can strongly perturb the optical mode if they are close enough to the waveguides.

2.2.17 Clad with thick Oxide

We deposit a thick oxide cladding both to protect the devices and to provide optical isolation from the environment. After the thin HTO step, the optical mode of the waveguide can still interact with the atmosphere above it, so we deposit an additional thick oxide cladding, typically an additional 2 μm. We use PECVD oxide because of its fast deposition rate and relatively high quality, ~100 nm/min. This process uses a combination of silane (SiH_4) and nitrous oxide (N_2O). Although PECVD processes are typically nonconformal and create films with residual hydrogen contamination, these effects are often negligible because the majority of the optical mode will interact with the HTO cladding layer beneath.

2.2.18 Define Facet

We define the input facet of the chip by dicing near the input, and then polishing to reduce roughness and to finely adjust the position of the facet. We use a K&S 7100 Dicing Saw tool to cut the individual chips from the wafer. The position of the cut will define the approximate position of facet. However, the edge defined by this cut is rough, so we carefully polish this edge with diamond pads of gradually reducing grain size in order to smoothen the facet. This also allows us to carefully adjust the distance between the facet edge and the nanotaper input of the optical devices.

2.3 Process Improvements

2.3.1 Grow BOX: Long Dry Oxidation

We increase the initial dry oxidation time to create a thicker high quality oxide near the optical waveguide mode. Dry oxidation (i.e. oxidation in an O_2 environment) yields an extremely high quality oxide, but the growth rate is extremely slow. Furthermore, as with most diffusion based processes, as the grown oxide thickness increases, the oxide growth rate decreases because the oxygen molecules must first diffuse through a thicker film before it can reach the silicon substrate, where it can react to grow more oxide. To give a sense of this rate decrease, at 1200°C, dry oxidation will take 1 hour to grow almost 200 nm, 1 day to grow 1 μm, and 1 week to grow almost 3 μm.

To overcome the slow rate of dry oxidation, wet oxidation is used (i.e. oxidation in an environment in which H_2O has been dissociated into H_2 and O_2). In this case, the H_2 acts as a catalyst in the reaction, which greatly enhances the growth rate, by as much as a factor of 5. The oxide is of slightly lower quality because of residual hydrogen within the film, but this level of material quality is often sufficient for optical devices.

However, mid-infrared (MIR) wavelengths are sensitive to residual hydrogen within the film, because many hydrogen bonded molecules have absorption resonances in the MIR (See Chapter 4). Although wet oxidation can provide sufficient material quality in the telecom and visible wavelength range, we must avoid employing wet oxidation for MIR applications. Therefore, we extend the initial dry oxidation step used during BOX formation to 5 hours, yielding ~0.5

μm, which should ensure that most of the optical waveguide mode will interact with the higher quality oxide. Because of time limitation and diminishing growth rate of oxidation, we continue with wet oxidation and then dry oxidation as detailed in Section 2.2.2.

2.3.2 Deposit Si_3N_4: Trench Definition, Argon Anneal

We define trenches in the wafer prior to deposition to prevent cracking from occurring. Although the previous process (see Section 2.2.3) could successfully grow films up to 750 nm without cracking, this was not necessarily repeatable. Even within the same furnace deposition, some wafers would crack whereas other wafers would not. In addition, even wafers that were crack free after film deposition would occasionally spontaneously crack over time, sometimes during device processing. This was especially problematic because it could significantly reduce device yield. To prevent this, we define trenches prior to film deposition around the edge of the wafer. These trenches prevent cracks that initiate at the edge of the wafer from propagating to the interior of the film. This is detailed further in Section 3.3. More complicated techniques can be used to define these trenches, but for simplicity and ease of fabrication, we manually use a diamond scribe to inscribe trenches into the wafer.

We also change the atmosphere of the annealing process that occurs mid-depostion (see Section 2.2.3). Instead of using ambient N_2 during annealing, we use argon. N_2, while a relatively stable gas, can still potentially react with devices. This is not problematic in itself, but if there is residual hydrogen in the film, the N_2 can potentially bond with the hydrogen within the material and

prevent it from escaping. The N—H bond is particularly problematic because it has a characteristic absorption in the MIR, and an overtone of this absorption also appears at telecom wavelengths[5]. Therefore, to prevent this, we use argon as the ambient annealing gas instead. Because argon is a noble gas, it is unreactive and should not alter the properties of the devices. Note that this is mostly a precautionary measure though; there has been no significant evidence that annealing with N_2 atmosphere increases the concentration of N—H bonds.

2.3.3 Spin Anti-Charging Layer: Removed

We remove the anti-charging layer step from the process. There was no significant change in device quality observed with and without the use of ESpacer. In addition, we can easily avoid stitching error (which the anti-charging layer was designed to ameliorate) by designing the CAD layout of our devices within a single write field of the e-Beam. In addition, the previous process had no cleaning step for the ESpacer itself, so there was possibility of contamination of devices. Because of the diminishing advantages of using ESpacer and the potential risks associated with its use, we choose to remove this step from the process.

2.3.4 Draw CAD: Rounder Polygons, Single Field Devices

We create CAD layouts that use more points per bend, so that polygons are less discretized and more “rounded”. The result of CAD layout are GDS files, which are composed of many polygons, which are themselves composed of

many points. However, because polygons have a discrete number of points, a perfect circle is impossible to describe, since one would require infinite points. Normally, one would simply describe a circularly shaped polygon with a very large number of point, and in most circumstances this would be a sufficiently close approximation to a circle. However, the GDS file standard has a default value of 199 for the maximum number of points used to describe any single polygon. For a sufficiently large circle, this number of points is insufficient to describe the circle, since the distance between each point scales with the radius. In fact, for our ring resonators of radius 46 μm, we can see this discretization when zoomed in on the coupling gap between the waveguide and the ring, as seen in Figure 2.2. Note that this discretization cannot be seen when viewed at larger scale, for example with a standard microscope. Although unnoticed by eye, this discretization creates "corners" which can scatter light during propagation. In addition, these "corners" appear as tight bends, which can radiate light from the waveguide.

We can easily resolve this issue by designing the CAD layout to include more points per bend. The GDS file default is 199 points per polygon, so we overwrite the default value to use 2000 points instead. This effectively smoothens the bends, allowing for lower loss bends. Although, even higher values can be used, they can also dramatically increase the GDS file sizes.

We also avoid stitching error during exposure by designing CAD layout such that devices are within the 1 mm by 1 mm write field of the JEOL. As mentioned in Section 2.2.5, stitching error during exposure can lead to misaligned patterned sections (Figure 2.3). When the misalignment is particularly bad, it can lead to a break in the waveguide, which can render devices unusable. How-

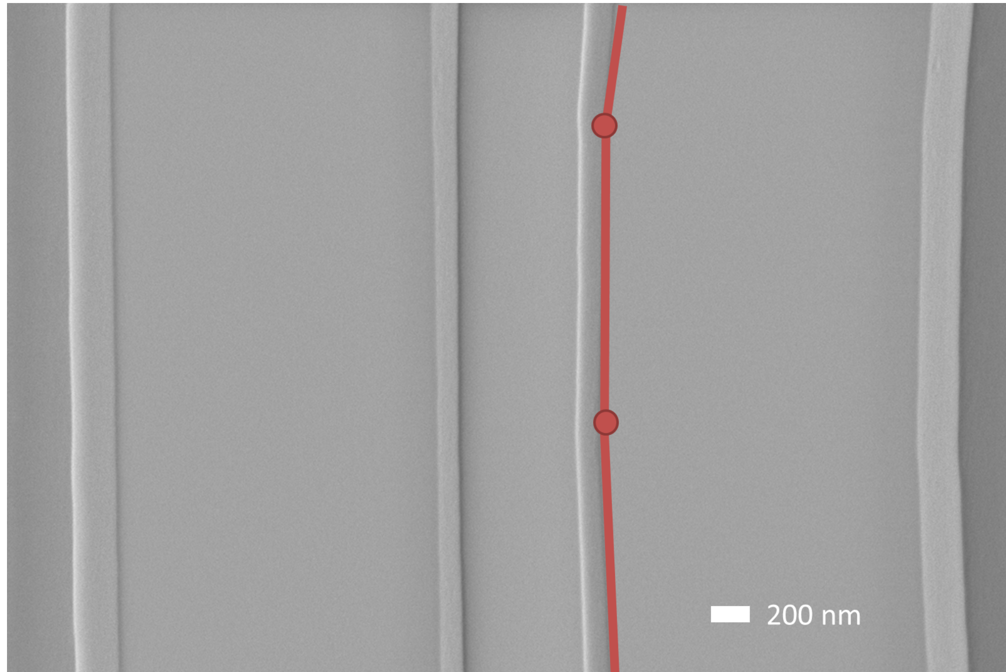

Figure 2.2: SEM of the coupling gap between a straight bus waveguide and a 46 μm ring resonator. Note the significant distortion of the rounded ring section on the right; we can see the curved section has been approximated by three different line segments (outlined in red). This distortion can only be seen on the SEM; when zoomed out far enough, these segments are small enough to appear perfectly circular.

ever, by compactly laying out devices into a single JEOL write field, we can avoid the need to stitch altogether, since stitching error mostly occurs between patterns located in multiple write fields. This is inconvenient because certain device topologies and multiple device variations can be difficult to fit within a single write field, but these challenges can be overcome with carefully thought out device layout.

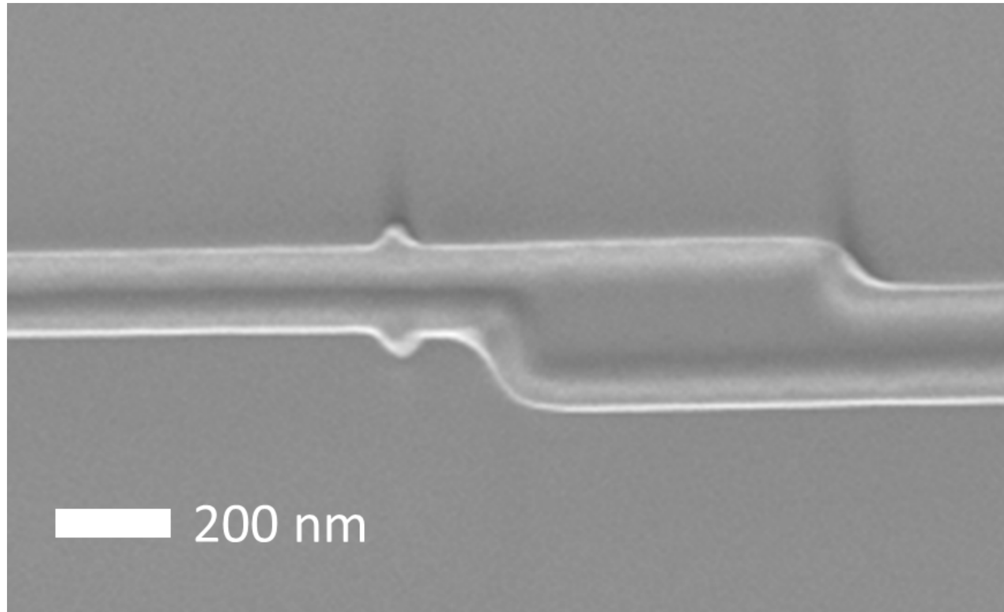

Figure 2.3: SEM of a line that suffered stitching error. Instead of a single continuous line, we see two lines, with the line on the right shifted down and left from its intended position.

2.3.5 Expose e-Beam Resist: Proximity Error Correction

We use proximity error correction (PEC) during JEOL file preparation to correctly dose areas of the device that have varying pattern density. As mentioned in Section 2.2.7, correct exposure dose is necessary for the resist to expose to completion and for the feature sizes to remain undistorted. However, the correct exposure dose for an isolated feature is higher than for a feature in a densely packed area of features. This is because a feature can experience partial exposure from other features nearby, which is termed the "proximity effect". However, this effect can be corrected for with PEC, which is a method for adjusting the dose to account for the proximity effect. First we use Sceleton™, a commercially available high-speed Monte Carlo simulation software provided by XLith, to simulate the electron trajectories through our film stack and then to calculate

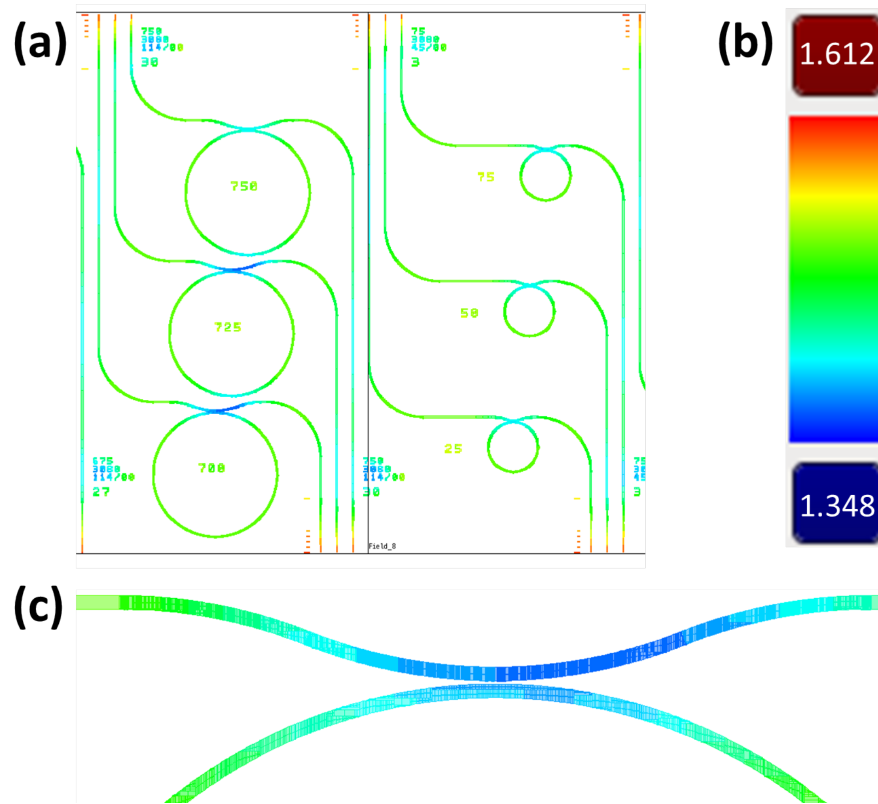

Figure 2.4: Screenshots of the results of PEC using BEAMER. A few ring resonators are shown in (a), scale bar of relative dose from 1.348 to 1.612 in (b), and an expanded image a coupling region in (c). Note that there is significant dose correction from the case of an isolated waveguide (green) in the nanotaper region (red) and the coupling region (blue) because of the change in the density of the pattern. Also note that the devices are placed within a single e-Beam write field (black), as explained in Section 2.3.4

the radial energy density distribution in the resist layer. Next, we input this numerical distribution into BEAMER, an e-Beam lithography software provided by GenISys, which then calculates corrected doses for the CAD layout (Figure 2.4).

2.3.6 Descum e-Beam Resist: Removed

We remove the descum step from the process. As mentioned in Section 2.1.5, oxygen plasma can have detrimental effects on the Si_3N_4 film. In fact, the devices demonstrated in [6] could only achieve high finesse values when oxygen plasma was removed from the process entirely. In addition, because of the increased oxygen flow used during the etching step of the process, any resist residue will be burned off very quickly during the etch step anyway, so the descum step is not essential. Because of the negative effects of descum, and the reduced need for it because of the oxygen-increased etch, we remove the descum step from the process.

2.3.7 Hard Bake e-Beam Resist: No Reflow

We lower the temperature of the hard bake step to 115°C to avoid reflow of the resist. The resist needs to be baked after developing in order to improve its selectivity against etching, but baking at too high a temperature can reflow the resist. Essentially, the resist melts and becomes dome shaped (Figure 2.5). This severely distorts the geometry of the waveguide, and we lose the ideal rectangular cross section.

Reflow is particularly problematic for the nanotapers of the devices. Because the nanotapers are designed to be very narrow, they have a very high aspect ratio. Features of high aspect ratio are much more likely to reflow, and when they reflow they distort more significantly from the original geometry. In practice, this creates nanotapers that are much wider than designed and partially etched on the top surface, which drastically reduces the size of the optical mode at

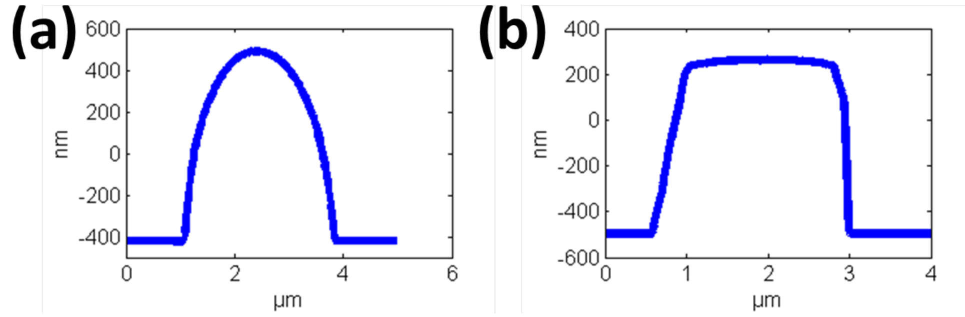

Figure 2.5: AFM scans of the resist after hard bake with (a) the previous process at 135°C and (b) the improved process at 115°C. The rounded shape in (a) is a characteristic signature of reflow, whereas the sharp vertical right edge in (b) signifies that the resist is no longer reflowing. Note that when there are sharp edges in the topology, we expect an asymmetric scan. This is an artifact of the AFM measurement, and is discussed further in Section 2.3.11

the nanotaper. This results in strong mode mismatch between the input optical beam and the nanotaper mode which increases the coupling loss. Typical facet losses with the previous process were 5-6 dB/facet, but with optimized processing we have achieved less than 1 dB/facet.

Although reflow techniques are sometimes used to smoothen the roughness of the resist, this applies mostly to the roughness along the cross section of the resist; roughness along the axis of propagation may not be significantly reduced, especially if there is no tensional force on the resist along the propagation direction. Therefore, we would ideally avoid reflow altogether, but avoiding a hard bake reduces the resist selectivity to the point that it can no longer survive the etch step. Therefore, we lower the baking temperature to 115°C and verify via AFM that the resist no longer reflows.

2.3.8 Etch Si_3N_4: Reduced Oxygen

We reduce the oxygen flow in the etch step to improve the selectivity of the resist during etching. Because of the lower bake temperature (see Section 2.3.7), the resist selectivity has decreased and can no longer survive the etch step. One solution is to increase the thickness of the resist, in order to compensate for the decreased selectivity. However, when this is attempted, the increase in resist thickness also increases the aspect ratio of the resist. As mentioned in Section 2.3.7, high aspect ratios are more likely to reflow. Even at the lower baking temperature of 115°C, an increased resist thickness reflows.

Therefore, we pursue another approach. Instead of increasing resist thickness to compensate for reduced etch selectivity, we increase the selectivity directly by reducing the amount of additional oxygen used in the etch recipe (see Section 2.2.11). Instead of using 4 sccm of oxygen, we use 3 sccm. This is still above the default value of 2 sccm, and we observe no additional resist polymerization during etching. Therefore, 3 sccm of oxygen is sufficient to reduce resist polymerization, which was the main purpose of increasing the oxygen content of the etch.

2.3.9 Etch Backside Si_3N_4: using Recessed Wafer (Optional)

We optionally remove the backetch step from the process. The backetch was originally included in the process as a precautionary measure against cracking, but there was no conclusive evidence at the time that this was necessary. Etching of the frontside actually relieves stress on the frontside of the wafer, so even if cracking would occur, it should mostly occur on the backside, which should not

affect device yield or quality.

Additionally, the backetch is a risky process because it requires the wafer to be laid face-down on the etch loader. At this point in the process, the devices are fully exposed to the environment, except for a thin layer of soft e-Beam resist protecting the top of the devices, so physical contact with the metal loader can easily damage devices. In fact, we often pattern multiple copies of devices specifically because of the lower yield in this part of the process. Because the backetch does not provide a necessary advantage and introduces heavy risks, we optionally remove this step from the process.

However, in some circumstances we do need to etch the Si_3N_4 from the backside. The stress imbalance between the films on the frontside and the backside of the wafer, especially if the wafer is double-side polished (see Section 4.5.3), can lead to extreme wafer bowing after the frontside film has been etched. This is usually insignificant for thinner films, but for thick films of Si_3N_4, bowing as large as 170 μm has been observed. Such a drastic variation in height across the wafer can lead to nonuniformity and misalignment in any photolithography steps later in the process. In practice, this leads to integrated heaters that have poor efficiency because heat is not being applied in close enough proximity to the waveguide due to misalignment. Etched facets also suffer because misalignment can place the input facet too close to the input nanotaper and the output facet too far from the output nanotaper (or vice versa), which can drastically reduce coupling efficiency into and out of the chip. For both heaters and etched facets, the bowed nature of the wafer also makes it impossible to align identically to all devices; inconsistent alignment occurs because we are mapping the flat plane of the photolithography mask to the curved surface of wafer.

We use a recessed wafer to aid in the etch of the backside Si_3N_4 film. As shown schematically in Figure 2.6, to prevent the devices on the frontside of the wafer from contacting a hard surface, we place the wafer face-down on a recessed wafer, such that the device region itself is not in contact with any surface. To accomplish this, we create a recessed wafer by deep etching into a silicon wafer. The etcher we use has a ring clamp that holds the wafer during the etching process, and this ring clamp naturally protects the wafer edge from being etched. Therefore, we can etch the majority of the silicon wafer area but still maintain a raised area a few millimeters wide around the edge of the wafer. At this point, we must be careful to etch the recess in the wafer deep enough such that the device region will not contact the center of the recessed wafer. Therefore, we must etch at least the bowing value of the device wafer, ideally 2 to 3 times the bow of the device wafer.

To adhere the two wafers together and to protect the device area from the environment during the etching process, we spin-coat thick photoresist around the edge of the wafer only. To accomplish this, we spin the wafer and then carefully dispense the photoresist through a pipet onto the edge of the wafer while it is spinning. We coat only the edge of the wafer because we do not want any photoresist residue to contaminate the currently exposed device area, and we only need the wafers to adhere at the points in which they will be in physical contact, namely the edges. We repeat this edge spin-coat procedure on the device wafer, soft-bake both wafers for 90 seconds at 90°C, and then carefully press the wafers together. At this point we must be careful not to press the wafers together in their centers, because we do not want the device region to come into physical contact with the recessed region.

We etch the backside of the film in CHF_3/O_2 plasma. Note that this etch is not critical because there are no devices on the backside, so in principal we can use any etcher with any gas chemistry. For ease of loading, we use an RIE etcher with lower power than the etcher used for etching the frontside. After etching, we gently separate the device wafer from the recessed wafer, using a razor blade to wedge the wafers apart if necessary. We clean the protective photoresist on the edge of the wafer by spinning the wafer and spraying acetone and isopropanol solvents. There are several methods to clean photoresist (see Section 2.1.5), but this method has the additional advantage of ensuring that any photoresist residue will be flung away from the device area in the center of the wafer, because the spinning wafer creates a radial flow away from the center. Any traces of remaining residue will be removed completely in the next stripping step.

2.3.10 Strip e-Beam Resist: Chemical Stripping

We strip the e-Beam resist using Hot Piranha solution (see Section 2.1.5). As mentioned in Section 2.3.6, oxygen plasma can be detrimental to device performance, so we choose to strip without oxygen plasma. However, acetone and isopropanol may not be strong enough to dissolve the e-Beam resist, which is notoriously difficult to remove. Therefore we choose to use Hot Piranha, which is an aggressive chemical solution that should be strong enough to remove the resist.

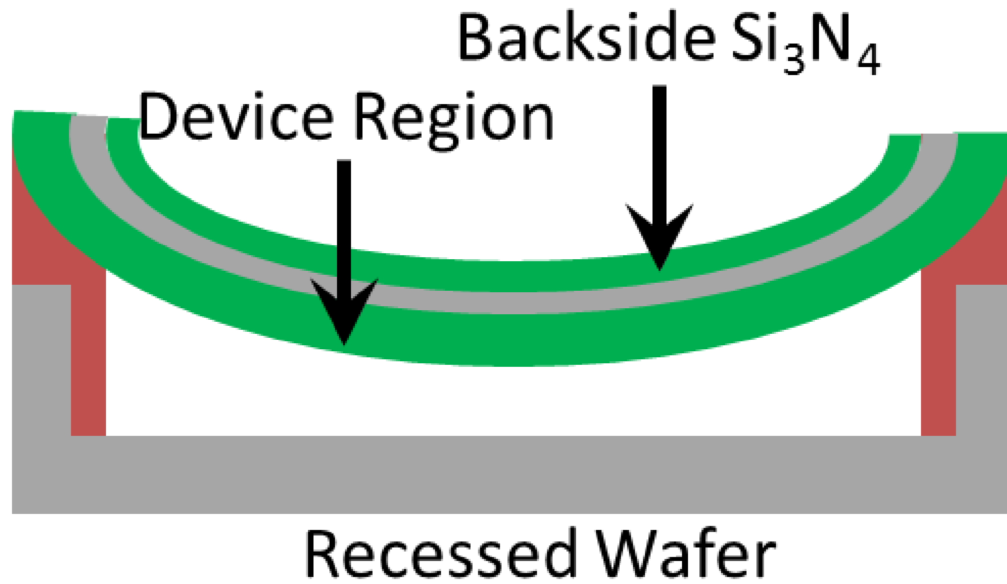

Figure 2.6: Schematic of the process used to prepare the device wafer for the backside etch using a recessed wafer. The device wafer is placed upside down on the recessed wafer, with photoresist (red) used to seal the wafers together. The gap between the device region and the recessed wafer prevents physical damage to the devices.

2.3.11 Geometry Measurement: Measure Waveguide Profile

In addition to the SEM, we also use the AFM to perform measurements of the device geometry. Although the SEM can provide high resolution measurements of the waveguide width, because it is a 2D measurement, it cannot provide reliable information about the height. Height information is important because it reveals if the waveguide etch depth is sufficient. We can roughly infer the etch depth by measuring the film thickness on the wafer using a FilMetrics F50-EXR system, which measures and fits interference fringes across a broad spectrum, but this does not reveal the local etch depth near the device itself. However, the AFM can provide full 3D information of the waveguide, so we can extract

information about the waveguide width, height, and sidewall angle, which can influence the dispersion of the waveguide and the coupling strength to higher order waveguide modes. As an additional advantage, the AFM can measure height with less than 1 Å precision, which can be used to measure the roughness of the top surface of the waveguide. This can reveal whether any of the chemical treatments have roughened the surface, or whether the top surface has been etched because the resist had been completely consumed during etching.

Although the AFM can provide more information than the SEM, this measurement can sometimes give artifacts that are not representative of the true geometry. The AFM technique is intended for measuring roughness and slowly varying topologies, but we are using this technique to interrogate a waveguide with steep edges and corners. A basic schematic of the AFM measurement technique is shown in Figure 2.7. In this technique, a sharp tip is scanned back and forth while tapping the surface, and the height position during the scan is recorded. If we use an angled tip, we can improve the accuracy while scanning in one direction while sacrificing accuracy when scanning in the reverse direction. Since we only typically record one scan direction anyway, we can choose to record the preferred scan direction. However, because the tip is asymmetric, even within the preferred scan direction, only one sidewall can be resolved precisely. In addition, because an actual AFM tip has a slightly rounded tip (as opposed to an ideally infinitely sharp tip), the corners appear slightly rounded as well. However, despite these distortions, we can still extract meaningful data from the AFM measurement. We can still measure the top width within a few 10's of nm precision, the height profile within a few Å's, and the sidewall angle within a few degrees.

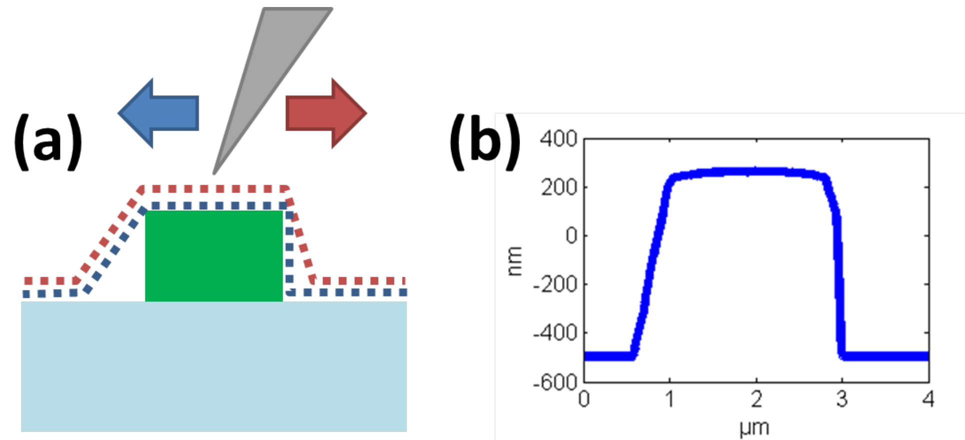

Figure 2.7: (a) Schematic of the AFM measurement and (b) actual data from an AFM measurement on a waveguide cross section. The AFM tip (grey) taps the surface as it scans left to right (denoted by red arrow and dotted red trace) or right to left (blue arrow and dotted blue trace). Note that for both traces, the left side of the waveguide cannot be resolved because of the angle of the AFM tip; as the tip scans, the right side of the tip eventually contacts the corner of the waveguide and the tip cannot access closer to the base of the waveguide. However, on the right side of the waveguide, the blue direction can resolve the sidewall, whereas the red direction cannot because the tip cannot lower itself fast enough to keep up with the steep sidewall. For the data in (b), we only record the blue trace.

2.3.12 Anneal Si_3N_4: Argon Anneal

We anneal the wafer at high temperature in argon atmosphere instead of nitrogen atmosphere. This anneal improves the optical quality of the top section of the Si_3N_4 film, as in Section 2.2.15, and we change the ambient gas to argon for the same reasons as in Section 2.3.2.

2.3.13 Define Facet: Etched Facets

We define the facets using photolithography and etching, and then dice to singulate individual chips, instead of polishing as in Section 2.2.18. There were several issues with the previous process of dicing and then polishing to define the facet position. Polishing is a manual technique that can only be performed on individual chips, or at most 2 chips at a time. This is both a time consuming and expensive process, since the diamond pads used in the polishing process wear down and must be replaced over time. As the number of chips on a given wafer has increased from at most 20 to almost 100, polishing can no longer scale. In addition, coupling loss from polished facets is very inconsistent between different chips, and even from device to device within the same chip. This is because the facet must be at most a few microns away from the nanotaper, but maintaining this small gap consistently across a 10 mm chip requires a leveling accuracy of 1/10,000. Unfortunately, our polishing process cannot achieve this because we manually level the chip. Therefore, the coupling loss can suffer dramatically because of a very slight angle of polishing. Furthermore, because the polished facet is at the edge of the chip, to maintain smoothness we cannot allow the edge of the chip to physically contact anything. This is not necessarily problematic, but it is very inconvenient when handling chips during experiments.

After fabrication of the wafer is complete, we perform the etched facet process to define the coupling facet (process flow shown in Figure 2.8). First we prepare the surface with Hot Piranha clean and Surpass 3000, and then spin-coat 7.5 μm (recently we have also successfully tried 5.25 μm) of MEGAPOSIT SPR220 photoresist. We bake the resist for 3 minutes at 115°C (carefully ramping the temperature at the beginning and end to prevent the resist film from

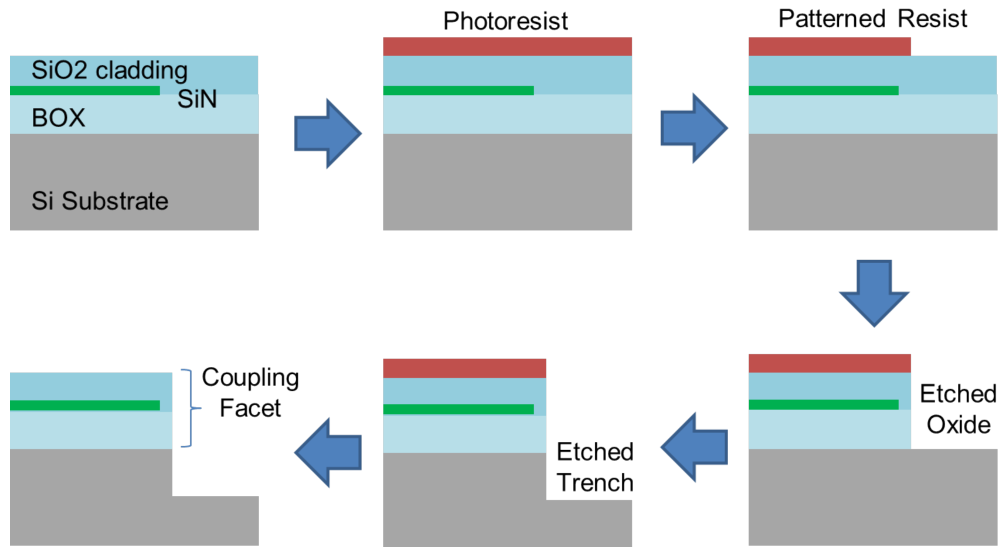

Figure 2.8: Schematic of the etched facet process flow (showing side view of nanotaper). First we coat and pattern photoresist, leaving a few μm gap between the patterned facet edge and the tip of the nanotaper. Then we etch into the cladding and bottom oxides, and then the silicon substrate to allow close access for lensed fibers or focused free-space beams. After stripping the remaining photoresist, we can dice to singulate the chips (not shown).

cracking), and then UV expose the resist (with an etched facet mask) on a Suss MicroTech MA/BA 6 Contact Aligner for 25 seconds (22 seconds for 5.25 μm resist). For resist films thicker than 4 μm, we must allow the resist to rehydrate for at least 35 minutes, so that water can diffuse back into the resist film and complete the photo-reaction. Following rehydration, we post-exposure bake the film again for 3 minutes at 115°C (ramping the temperature as before). We develop the resist manually via immersion in AZ® 300 MIF developer for 3 minutes, with agitation every 30 seconds. Immediately following development, we rinse spray the wafer with water and then dry with nitrogen. Before etching, we remove the edge bead of resist with a cotton swap and acetone. This completes the patterning step of the etched facet process.

After patterning the resist, we transfer the pattern into the silicon oxide and silicon substrate via etching. For the oxide etch, we use CHF_3/O_2 chemistry on an (ICP)-RIE etcher. We first clean the etching chamber for 10 minutes with an oxygen plasma, and then etch the sample in steps of 4 minutes for up to 30 minutes. After each 4 minute etch, we unload the sample to the loadlock chamber to allow it to cool. This is critical to prevent the resist from burning during the high etch chamber temperatures that occur during a long etch step. Etch steps of 4 minutes were the maximum etch time before burning occurred; 5 minute and 6 minute etch steps showed noticeable roughening of the resist after several etches. After a total of 30 minutes of etching, we clean the etching chamber again for 10 minutes, and then continue etching until all of the oxide has been etched. Once the oxide is etched, we etch the silicon substrate using a standard Bosch fluorine process on an (ICP)-RIE etcher. We etch the silicon to a depth of at least 125 μm, because that is twice the lensed fiber radius of 62.5 μm. This will ensure that the silicon substrate will not block the lensed fiber from accessing the coupling facet. After etching the silicon, we strip the resist in a high power (1000 W) oxygen plasma resist strip tool for 10 minutes. We use the high power and long strip time to ensure that hardened resist and polymer formed during etching are removed completely. After this point, the wafer is ready for dicing.

2.4 Optimized Etch Process

2.4.1 Etch Chemistry Optimization

We develop an optimized Si_3N_4 etch[1] in order to decrease sidewall roughness and to reduce sidewall angle. Both of these effects are important for comb generation, especially in the shorter wavelength ranges (see Section 5.5).

Because of poor etch selectivity to e-Beam resist, we use a SiO_2 hard mask. The hard mask is deposited on top of the Si_3N_4 film, and then resist is patterned on top of the hard mask. The resist pattern is transferred into the hard mask via a standard oxide etch, and then the hard mask pattern is transferred into the Si_3N_4 film via the optimized etch. In order to increase the etch selectivity of the optimized etch to SiO_2, nitrogen is added to the traditional CHF_3/O_2 chemistry [7]. After optimizing gas flow rates, bias voltage, and pressure, the final gas flow rates for the optimized etch are 47 sccm of CHF_3, 7 sccm of N_2, and 23 sccm of O_2. This high flow rate of oxygen is the reason the e-Beam resist has poor selectivity, and why we must resort to using an oxide hard mask.

2.4.2 Process Modifications

The optimized etch requires an oxide hard mask and has different etch rates and etch selectivities, which requires significant modification of several parts of the fabrication process. In modifying the fabrication process, we must first

[1]Much of the etch process development was done by Alex Bryant through the National Science Foundation (NSF) Research Experiences for Undergraduates (REU) program, under the guidance of Dr. Yoon Ho Daniel Lee and Dr. Jaime Cardenas

carefully select appropriate thicknesses for the SiO_2 hard mask, and then the e-Beam resist thickness. The following calculations are for etching through 730 nm of Si_3N_4. The optimized Si_3N_4 etch has a selectivity of 1.95 to SiO_2, so in order to etch through 730 nm Si_3N_4 as well as an additional 146 nm (overetch by 20% to resolve small gaps), a minimum of $730 \cdot 1.2/1.95 = 449$ nm of SiO_2 hard mask would be required. We choose a slightly thicker hard mask of 550 nm, in order to account for fabrication variation. The oxide etch we will use has a selectivity of 1.5 for oxide to resist, which corresponds to a minimum of 550/1.5 = 367 nm of resist. We choose a convenient spin-coat speed to give ~ 360 nm of resist. Note that for the oxide etch, we will not be overetching, in order to maximize the amount of Si_3N_4 etched with the optimized etch.

The processing is similar to the improved process detailed in Section 2.3, but with modifications. After film stack creation (see Section 2.2.3), we deposit the 550 nm SiO_2 hard mask using PECVD oxide. Then, when spin-coating e-Beam resist (see Section 2.2.4), since we require thinner resist, we spin-coat a less viscous dilution of ma-N (ma-N 2403) at spin speed of 2000 rpm (ramp 500 rpm/s) for 60 seconds. Because the resist is thinner, we require shorter develop time (see Section 2.2.8). We develop the resist for 60 seconds using an automated Hamatech-Steag Wafer Processor with AZ®726 MIF Developer. Later measurements reveal that this develop time yields slightly overdeveloped features. We pre-compensate for this by increasing feature sizes in CAD, but a shorter develop time may be more appropriate, although overdeveloping has not been shown to be a significant source of loss. Because we no longer require thick resist, we also remove the hard bake step entirely (see Section 2.3.7). The resulting decrease in etch selectivity has already been accounted for in the calculations above. At this point, we etch the SiO_2 hard mask with the standard

CHF_3/O_2 (with gas flow rate 52/3) chemistry, and then the Si_3N_4 with the optimized $CHF_3/N_2/O_2$ chemistry. Both of these etches are performed on an ICP-RIE tool. The final modification occurs after the resist strip (see Section 2.3.10). After stripping the resist, we also strip the remaining oxide hard mask in dilute HF (100:1) for 6 minutes (with constant agitation to ensure uniformity).

As an optional step, additional roughness reduction can be achieved after stripping the oxide mask by slightly oxidizing the surface using Hot Piranha clean, and then stripping the thin oxide in the same HF dilution for 3 minutes. This roughness reduction can be repeated several times, but one must be careful not to etch enough oxide to undercut the narrow nanotaper region.

CHAPTER 3

OVERCOMING STRESS LIMITATIONS FOR HIGH Q

3.1 Introduction

Silicon nitride (Si_3N_4) ring resonators are critical for efficient and compact on chip optical routing [8, 9, 10], frequency combs [11, 12, 13, 14], and high precision sensing [15, 16, 17, 18] , however the intrinsically high film stress of silicon nitride has limited both the optical confinement and quality factor (Q) of ring resonators. Whereas the silicon and silicon dioxide platforms generally suffer from high losses or delocalized optical modes, the Si_3N_4 platform provides advantages of both high confinement and high Q. High Q disks have also been demonstrated in Si_3N_4 [19] but disks have larger mode volumes and are challenging to dispersion engineer for nonlinear applications. Si_3N_4 is also a deposited material, which enables seamless integration with other material platforms. However, the high film stress of Si_3N_4 prevents thick (>400 nm) films of high optical quality from being deposited; catastrophic cracking occurs, severely limiting device yield. In principle low stress nitride films can be grown thicker with plasma enhanced chemical vapor deposition (PECVD) and modified low pressure chemical vapor deposition (LPCVD) processes, but these deposition chemistries yield films with stronger material absorption caused by dangling H and O bonds with the Si and N in the films.[1]

[1]Portions of this chapter are reproduced from [20]

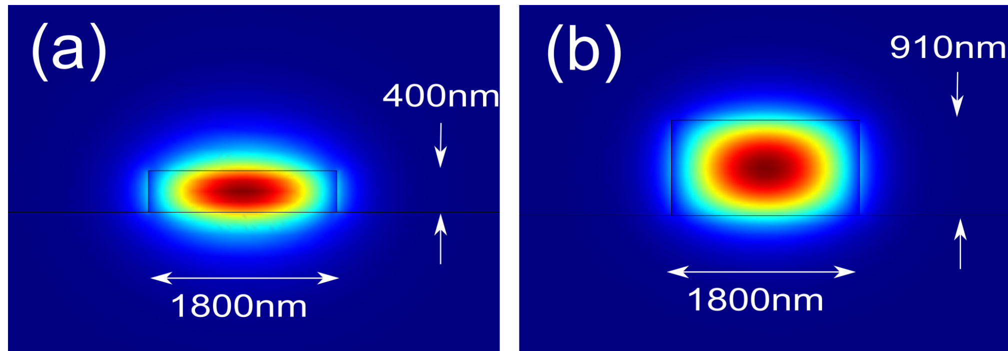

Figure 3.1: Transverse electric (TE) mode simulations at 1550 nm wavelength for the (a) 400 nm x 1800 nm and (b) 910 nm x 1800 nm waveguides with 71% and 93% modal confinement, respectively. Less of the optical field interacts with the waveguide boundaries for the taller waveguide (b).

3.2 Loss Reduction

Thick films, limited to date by stress, would enable high confinement and high Q. Thick films lead to smaller optical mode overlap with the boundaries of the waveguides (responsible for scattering losses) leading to lower losses. This can be observed in Figure 3.1 where we show the mode profile for a mode confined in two different waveguide thicknesses. Figure 3.1a shows the mode confined in a waveguide with a traditional thickness of 400 nm limited to date by stress. One can see that the mode overlaps significantly with the boundaries of the waveguide. Figure 3.1b shows the mode confined in a waveguide with a much higher thickness of 910 nm. One can see that very little of the mode overlaps with the boundary of the waveguide. Note that increasing the size of the waveguide increases the number of modes supported; however these higher order modes are only weakly excited.

Previous high Q Si_3N_4 ring resonators have circumvented film stress issues by exploiting either highly delocalized optical modes with extremely thin films

[21] or highly confined modes within film stress limits [12]. High Q ring resonators based on extremely thin Si_3N_4 films can avoid film stress issues, but they suffer from highly delocalized optical modes, requiring millimeter-scale bending radii and up to 15 μm of silicon oxide cladding. In addition, these resonators only support the transverse electric (TE) mode which prevents integration with devices that support the transverse magnetic (TM) mode. High confinement ring resonators based on thicker films can be achieved using high temperature deposition and anneal to relieve film stress, but films greater than 750 nm in thickness remain challenging.

3.3 Crack Isolation Trenches

In order to overcome the stress limitations of Si_3N_4, we strategically place mechanical trenches to isolate the photonic devices from propagating cracks. Physical shocks near the edge of the wafer, which occur often during handling of the wafer, can provide enough energy to induce cracking of the stressed film. Once initiated, these cracks originating from the edge of the wafer propagate continuously in a uniform stress field, terminating only once they encounter crack resistance at the edge of the wafer or at another crack boundary. We introduce trenches around our devices that terminate cracks before they can spread to our device region (shown in Figure 3.2). A single trench does not guarantee crack termination however [22]. Overstressed films store energy in the enhanced acceleration of the crack and the extended penetration into the substrate. With this stored energy, cracks can overcome the crack resistance of a single trench and continue propagation. To increase crack resistance, we create between two and five parallel trenches to ensure crack termination.

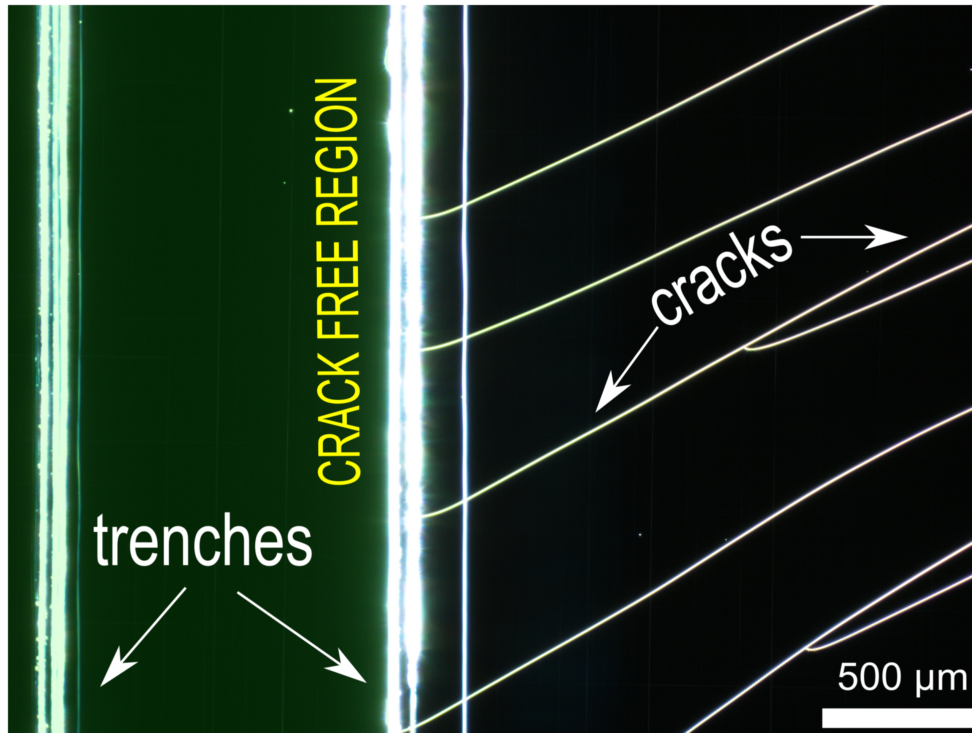

Figure 3.2: Microscope images in the dark field showing crack propagation terminating at a trench created with a diamond scribe. The film to the left of these trenches is crack free.

We define a series of trenches around the edge of the wafer before deposition of the Si_3N_4 film to prevent crack propagation. Beginning with a thermally oxidized 4 inch silicon wafer, we lightly scribe a series of lines into the silicon oxide surface to define a 5 cm by 5 cm rectangular region in the center of the wafer. This rectangular region will be the crack free region in which we pattern our photonic devices; elsewhere, the film will crack. Note that for ease of processing and throughput we define trenches with a diamond scribe, but in principle one can define more sophisticated trenches with photolithography and etching. Etching may actually improve the crack resistance of these trenches because of the increased roughness on the etched surfaces [22]. In addition, photolithography could be used to define trenches only at the wafer periphery to enlarge the area of the crack free region. Following trench definition, we proceed with

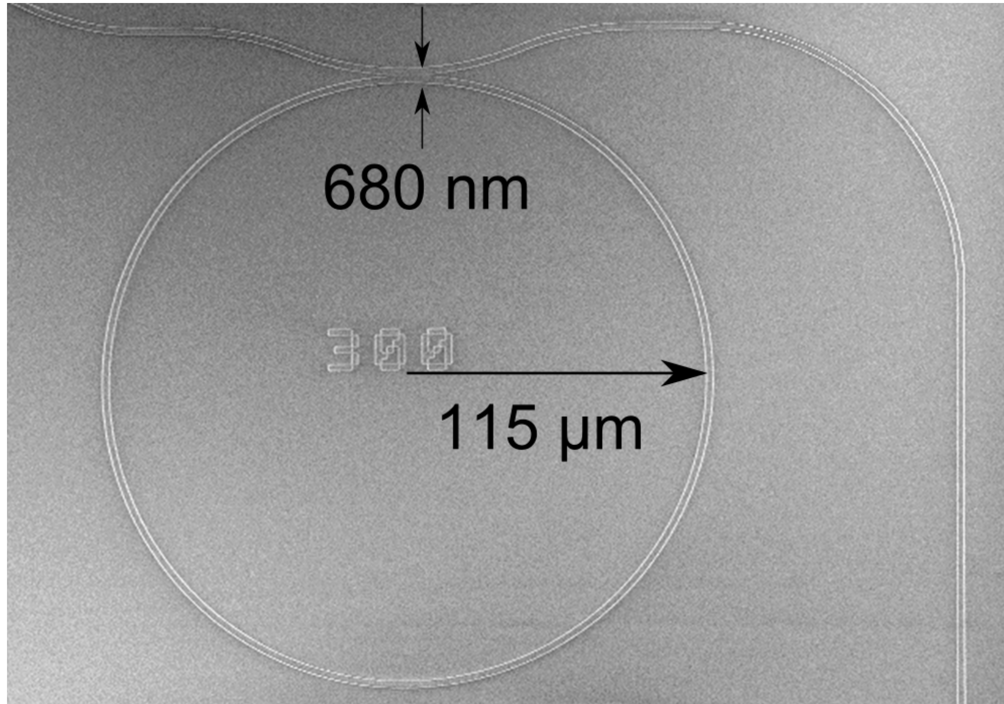

Figure 3.3: Scanning electron microscope (SEM) image of the resonator.

device fabrication as described in [12]. After deposition of 910 nm of Si_3N_4, in steps of 400 nm and 510 nm, we pattern devices with electron beam lithography using ma-N 2405 resist, post exposure bake for 5 minutes at 115°C, and etch in an inductively coupled plasma reactive ion etcher (ICP RIE) using CHF_3/O_2 chemistry. After stripping the resist, we anneal devices at 1200°C in a nitrogen atmosphere for 3 hours. We clad devices with 250 nm of high temperature silicon dioxide (HTO) deposited at 800°C followed by 2 μm deposition of silicon dioxide using plasma enhanced chemical vapor deposition (PECVD). The fabricated device is shown in Figure 3.3. Note that our trench definition method is not specific to this process; it can be applied to any highly stressed film in which cracks are initiated near the edge of the substrate.

3.4 High Q Measurement

We measure an intrinsic quality factor of 7 million, the highest quality factor reported to date for high confinement Si_3N_4 ring resonators; this quality factor corresponds to an ultra-low propagation loss of 4.2 dB/m. The ring resonator measured has a radius of 115 μm, a coupling gap of 680 nm, and a cross section of 910 nm tall by 1800 nm wide. We couple a tunable laser light source, transmitted through a polarization controller, into the inverse nanotaper of our device using a lensed fiber. We collect the output of the ring resonator through another inverse nanotaper and collimating lens. After passing the output through a polarizer, we monitor the output on a photodetector. In order to measure a single resonance, we finely scan the laser frequency by applying a triangular-wave voltage signal to the piezoelectric transducer of the laser, while monitoring the photodetector signal on an oscilloscope. We calibrate the voltage-frequency conversion with respect to a free space bowtie cavity. We observe some higher order mode resonances (shown in Figure 3.4), but these resonances have very low extinction, suggesting that most of the optical power is in the fundamental mode. Minimal higher order mode excitation is expected because we design our waveguides to support few modes: five TE modes and four TM modes. From the single resonance scan normalized to the maximum value, we measure a resonance linewidth of 36 MHz and resonant transmission of 26% (shown in Figure 3.4), corresponding to an intrinsic quality factor of 7 million for TE polarization. For TM polarization we measure a Q of 4 million. The Q for TE is higher because the TE mode has higher optical confinement and effective index, so the mode suffers less scattering and bending loss.

We calculate the propagation loss within the ring to be 4.2 dB/m and we

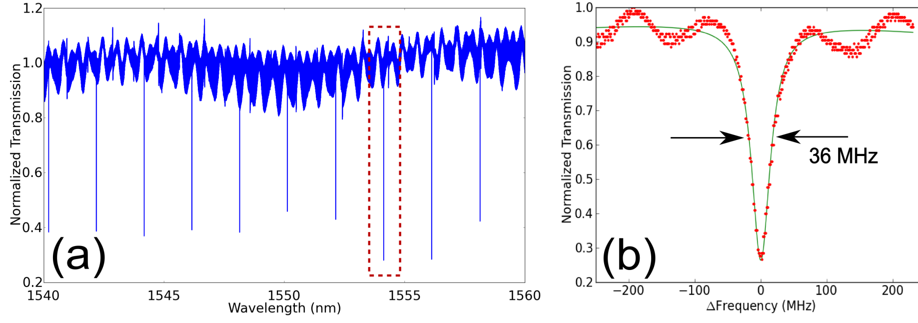

Figure 3.4: (a) Transmission spectrum with the finely scanned resonance outlined in red. (b) Resonance with 36 MHz linewidth corresponding to an intrinsic Q of 7 million.

estimate the absorption loss to be 25% of this loss, suggesting that the Q can be further improved with increased optical confinement. We calculate propagation loss using the relation [23]

$$\alpha = \frac{2\pi n_g}{Q\lambda_0} = \frac{\lambda_0}{Q \cdot R \cdot FSR}, \tag{3.1}$$

where n_g is the group index, λ_0 is the resonant wavelength, R is the radius of the ring resonator, and FSR is the free spectral range. For our device with ring radius of 115 μm, FSR of 2.0 nm, and resonant wavelength of 1554.8 nm, we calculate a propagation loss of 4.2 dB/m. This is the lowest loss reported for high confinement waveguides. We estimate the proportion of loss due to material absorption using Borselli's method [24]. Because silicon nitride has negligible nonlinear loss, we can assume that resonance shifting is dominated by thermal effects caused by material absorption. We use the resonance shift as a function of dropped power in [25] and simulated values for thermal conductance and thermo-optic coefficient to calculate an absorption loss of 1.0 dB/m for the devices in [25]. Because the film deposition process in [25] is identical to the

process used in this work, we can assume the same absorption for our devices, which accounts for 25% of the propagation loss. Therefore, the Q is not material limited and can be further improved with increased optical confinement and film deposition optimization.

3.5 Summary

We demonstrate a high quality factor of 7 million in a high confinement Si_3N_4 ring resonator using crack resistant trenches to overcome stress limitations of thick Si_3N_4 films. Our high Q devices herald advances in low loss optical routing, low power threshold nonlinear optics, and high sensitivity sensors. We have also overcome film stress limitations for Si_3N_4, revealing a new design space for integrated optics and microelectromechanical (MEMS) devices that has been unexplored to date.

CHAPTER 4

FREQUENCY COMB GENERATION IN THE MID-INFRARED

4.1 Introduction

Microresonator-based parametric frequency combs are of interest for their applications to precision frequency metrology, optical clocks, and absorption spectroscopy [11, 14, 26, 27, 16] because of their narrow linewidths and precise frequency spacing. Comb generation in the mid-infrared (MIR) wavelength range (2 – 20 μm) is of particular interest for spectroscopy of characteristic molecular vibrational transitions and for trace gas sensing within the Earth's atmospheric transparency window [28]. Some MIR comb sources have been demonstrated in fiber lasers, mode-locked lasers and optical parametric oscillators [29, 30, 31], but these systems systems are either bulky or limited in power per comb line. Microresonator-based combs in contrast provide compact, robust systems that require relatively low operating power, but few have been demonstrated in the MIR [32, 33, 34, 35]. Although several microresonator-based combs have been demonstrated in telecom wavelengths, to date few fully integrated combs have been generated in the MIR.[1]

4.2 Dispersion Engineering

Although there exist several transparent materials (for example crystalline fluorides) in the MIR, these materials are difficult to dispersion engineer. The para-

[1]Portions of this chapter are reproduced from [36]

metric four-wave mixing process that is responsible for comb generation typically requires anomalous group velocity dispersion (GVD) to enforce proper phase matching. In telecom comb generation, this is most often done by engineering the geometry of the resonator to modify the waveguide dispersion of the resonator. However, many low-loss MIR materials have low refractive indices, which results in lower index contrast. This reduces the impact of waveguide dispersion on the overall dispersion of the resonator. Because the waveguide dispersion can be geometrically tuned whereas other sources of dispersion are fixed by material properties, engineering overall anomalous dispersion is challenging.

4.3 Optical Characterization of Si_3N_4

Although many thin film materials, in particular Si_3N_4, have relatively high refractive indices, lack of material characterization in the MIR wavelength range has made dispersion engineering challenging. The optical properties of Si_3N_4have been characterized in the telecom wavelength range and shorter wavelengths [14,15], but not in the MIR. This is mainly because commercial ellipsometers available can typically only characterize films below the wavelength of 2μm, due to limitations of the equipment's light source. Beyond this range, the film properties are typically extrapolated from the Sellmeier coefficients derived from the measurable range of the ellipsometer. Although Sellmeier equations are considered valid within the transparent region of a material, this is only true if all absorption resonances contributing to the optical properties are included in the Sellmeier equation. However, $Si_3N_4$is known to have a strong absorption peak near 10μm, which can strongly influence the optical

properties at shorter wavelengths. Therefore, extrapolation of Sellmeier coefficients is insufficient; we must properly characterize the Si_3N_4 film in the MIR to include influence of MIR absorption resonances.

We work with J.A. Woollam Co., the leading manufacturer of spectroscopic ellipsometers, to characterize the optical properties of Si_3N_4. We send three samples for characterization: one sample of uncoated silicon, one sample of 4.6 μm of thermally grown SiO_2 on silicon, and one sample of 340 nm Si_3N_4 on 3.1 μm of thermal SiO_2 on silicon. The Si_3N_4 sample was deposited via low pressure chemical vapor deposition (LPCVD), and then annealed for 3 hours at 1200°C. J.A. Woollam then measured these samples with their M-2000 and IR-VASE instruments over the 193-1690 nm and 1.7-33 μm wavelength ranges, respectively. The data was fit to Lorentzian and Gaussian oscillator models (Figure 4.1), and then simultaneously fit over both ranges to obtain the following Sellmeier equation for Si_3N_4:

$$n_{SiN}^2 = 1 + \frac{3.0249\lambda^2}{\lambda^2 - 135.3406^2} + \frac{40314\lambda^2}{\lambda^2 - 1239842^2}. \tag{4.1}$$

This equation is valid over the wavelength range 310-5504 nm, with λ in units of nm. Another Sellmeier equation was obtained for SiO_2, which matched literature values well. We use these equation to model the Si_3N_4 and SiO_2 layers for dispersion engineering in the MIR.

4.4 Growing Thick Si_3N_4 Films

Because of the longer wavelength in the MIR, film thicknesses required for anomalous dispersion must be thicker; however intrinsic film stress in Si_3N_4 has restricted the thickness of Si_3N_4 films. We engineer the dispersion of

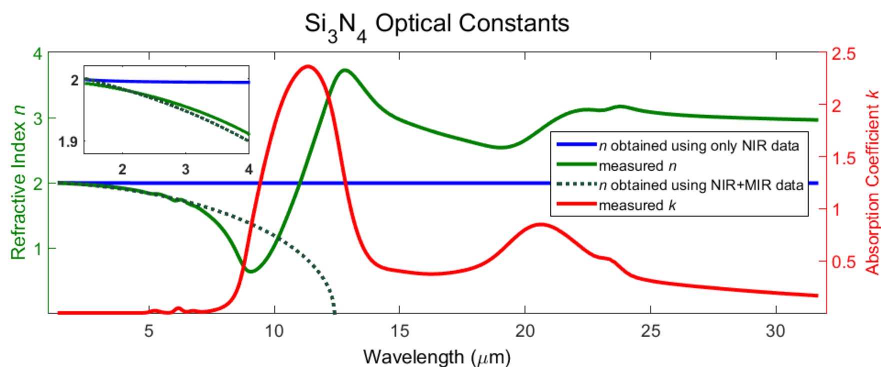

Figure 4.1: Refractive index n and extinction coefficient k for the wavelength range 1.4-32 μm. Extrapolation from NIR Sellmeier equations (blue) shows no influence from the MIR absorption peak, as expected. However, the measured absorption peak near 10 μm (red) strongly influences the measured refractive index (green), and the fitted Sellmeier equation (dotted green) agrees well with the measurement in the spectral range between 1.4 and 4 μm (see inset). As shown in the inset, at shorter wavelengths, even as far as the telecom wavelength range, the refractive index is significantly influenced by the MIR absorption peak.

our resonator by choosing the height and width of the rectangular waveguide cross-section to yield anomalous GVD. However, for certain waveguide heights (which are in practice determined by the film thickness), anomalous GVD is impossible to achieve for any waveguide width. This is because the optical mode of the waveguide is not confined enough to the core in order to achieve sufficient waveguide dispersion. Therefore, as wavelength increases, we require larger waveguide heights, which correspond to thicker films. However, these film thicknesses are often unavailable because intrinsic film stress causes the films to crack at large thicknesses. Once the films have cracked, they are optically unusable because the crack sites are significant sources of loss.

We achieve film thicknesses required for anomalous GVD using crack isola-

tion trenches detailed in [20] and in Section 2.3.2. These trenches are made using a diamond scribe prior to Si_3N_4 film deposition. When cracks form, they cannot propagate past the trench, resulting in a large crack free region of the wafer. This technique allows us to access film thicknesses beyond the traditional limit of 750 nm [12], which is required for achieving anomalous GVD in the MIR. For this work, we use a film thickness of 950 nm and a waveguide width of 2.7 μm.

4.5 Improving Absorption Loss

Another major challenge for comb generation in the MIR has been high optical loss, particularly from material absorption. Many of the materials that have been used for frequency comb generation in the telecom wavelength range (1.55 μm) have vibrational absorption bands in the MIR. In particular, trapped hydrogen impurities within thin films can introduce absorption bands in the MIR. In addition, multiphoton absorption can become a significant source of loss in many materials. Multiphoton absorption can excite free-carriers which can exacerbate losses, particularly in silicon. This problem has been ameliorated in silicon with an integrated diode to extract the generated carriers [32]. In this case, the authors successfully generate a MIR frequency comb in silicon, but this solution involves a more complex fabrication process as well as active extraction of carriers.

4.5.1 Absorption Loss Estimation

We develop a method for estimating material absorption losses as a tool for improving material absorption for the MIR. Adapting the method developed by Borselli et. al [37], we estimate the amount of absorption by measuring the resonance shift as a function of power. Because Si_3N_4 has negligible nonlinear losses in the MIR and no free-carriers, resonance shift is dominated by thermal effects. We can therefore link this thermal resonance shift $\Delta\lambda_{th}$ to the increase in absorbed optical power ΔP_{abs} via the group index n_g, the low power resonance wavelength λ_0, the effective thermo-optic coefficient $(dn/dT)_{eff}$, the thermal conductance κ_{th}, and the round-trip path length of the resonator L:

$$\Delta\lambda_{th} \overset{n_g/\lambda_0}{\Rightarrow} \Delta n \overset{(dn/dT)^{-1}_{eff}}{\Rightarrow} \Delta T \overset{\kappa_{th} L}{\Rightarrow} \Delta P_{abs}, \tag{4.2}$$

The values for $\Delta\lambda_{th}$ and λ_0 are measured experimentally, whereas n_g, $(dn/dT)_{eff}$, and κ_{th} are determined via simulation of the resonator cross section and known material constants. To calculate $(dn/dT)_{eff}$, we weight the different thermo-optic coefficients of the different materials of the resonator cross section (in this case silicon nitride and silicon dioxide) by the optical mode confinement in that material. For the geometry used in this work, $(dn/dT)_{eff}$ is dominated by $(dn/dT)_{SiN}$. From characterization at low optical power, we can determine the dropped power P_d, corresponding to the total amount of power lost in the resonator, from the minimum resonant transmission T_{min}:

$$\Delta P_d = (1 - T_{\min})\Delta P_{in}. \tag{4.3}$$

Combining Eq. 4.2 and 4.3, we obtain an expression for the ratio of absorption loss to total loss, η_{abs}:

$$\eta_{abs} = \frac{\Delta P_{abs}}{\Delta P_d} = \frac{\kappa_{th} L n_g \Delta\lambda_{th}}{\lambda_0 \left(\frac{dn}{dT}\right)_{eff} (1 - T_{\min})\Delta P_{in}}. \tag{4.4}$$

As we improve the material quality and device processing for MIR applications, we use η_{abs} as a tool to determine if absorption is the dominant loss mechanism.

4.5.2 Cladding Anneal

We improve absorption losses post-fabrication with a high temperature anneal and verify the improvement with absorption estimation. As a first attempt, we fabricate resonators as detailed in [20], with a cross section of 910 nm tall by 2.4 μm wide and round-trip path length of 1.8 mm. For this geometry, we determine via simulation n_g=2.12, $(dn/dT)_{eff}$=3.5×10^{-5} K^{-1}, and κ_{th} =3.7×10^{-5} W/Kμm at λ_0=2.6 μm. From low power characterization (Figure 4.2), we measure an intrinsic quality factor (Q) of 55,000. From high power characterization, we measure a resonance shift of 0.5 nm for 115 mW increase in optical power, resulting in η_{abs} =0.9, which indicates that losses are heavily dominated by absorption. This absorption may be due to residual hydrogen in the silicon nitride core and silicon oxide cladding, since hydrogen bonds are known to absorb in the MIR. We drive out this residual hydrogen by annealing the devices at 1100°C in argon atmosphere for 13 hours. We repeat low power (Figure 4.2) and high power characterization on the same resonator, and measure a Q of 200,000, and η_{abs}=0.6. Although the increase in Q demonstrates that we have successfully improved the material quality in the MIR, η_{abs} suggests that losses are still dominated by absorption.

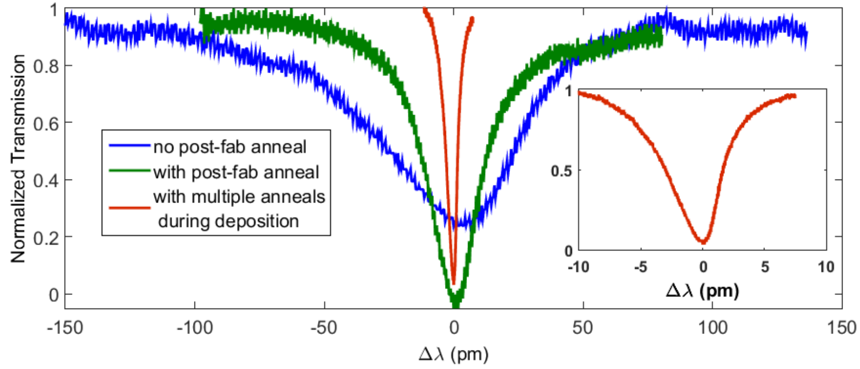

Figure 4.2: Resonance spectrum measured around λ_0=2.6 µm for devices fabricated with single anneal during Si3N4 film deposition but without post-fabrication annealing (blue), with post-fabrication annealing (green), and multiple annealing (red) during Si3N4 film deposition. For devices with cross section 910 nm tall by 2.4 m wide, the Q improves from Q=55,000 with single anneal during deposition (blue) to Q=200,000 after a long post-fabrication anneal for 13 hours at 1100C (green). The resonance extinction increases as expected, since reduction in losses transitions the resonance from under-coupled to critically-coupled regime. With multiple annealing during film deposition (red, inset) of devices with cross section 950 nm tall by 2.7 m wide (the devices used for comb generation in this work), the Q improves to Q=1,000,000.

4.5.3 Mid-Deposition Anneal

We further improve absorption loss in the MIR by performing several high temperature anneals during film deposition, and we counteract resultant stress imbalance using double-side polished wafers. Because losses remain dominated by absorption following post-fabrication annealing, we hypothesize that annealing successfully drives out residual hydrogen from the silicon oxide cladding, but not from the silicon nitride core, since silicon nitride is an effective diffusion barrier. Hydrogen within the silicon nitride core will be prevented from diffusing to the nitride-oxide interface, where it can then outgas from the

film. We perform multiple anneals during film deposition (Figure 4.3) to allow residual hydrogen to outgas before the film can become too thick to prevent hydrogen from diffusing to the film boundaries. We deposit a total of 950 nm Si_3N_4 via low pressure chemical vapor deposition (LPCVD) at 800°C in layers of approximately 300 nm thickness, with an anneal of 1200°C in argon atmosphere for 3 hours between each deposition layer. However, when processing on single-side polished (SSP) wafers, the imbalance in film stress between the frontside and backside of the wafer leads to wafer bowing of up to 170 μm on a 4 inch wafer after the intermediate anneal step. This extreme wafer bow precludes further processing, because electron beam lithography tools cannot properly expose on wafers with large height variations. In addition, photolithography processes suffer from nonuniformity across wafers with extreme wafer bow. To prevent wafer bowing, we instead process on double-side polished (DSP) wafers. Although the films on the frontside and backside remain stressed, the stresses are balanced such that the wafer no longer bows. In order to maintain balanced stress, we must also process the backside throughout fabrication, as detailed below.

We fabricate Si_3N_4 microring resonators (Figure 4.3) with a record Q of 1.0 $\times 10^6$. We begin fabrication with double-side polished silicon wafers, and then oxidize 4.5 μm of silicon oxide. Using a diamond scribe, we define crack isolation trenches as in [20]. We then deposit a total of 950 nm Si_3N_4 via LPCVD and anneal cycling, as mentioned above. We then proceed with fabrication as detailed in [20]. Following deposition of 500 nm of high temperature oxide (HTO) cladding, we etch the Si_3N_4 film on the backside of the wafer, in order to balance film stress between the frontside and the backside of the wafer. This is necessary to prevent excessive wafer bowing after annealing in the next step. We anneal

again in order to drive out hydrogen impurities from the third layer of Si_3N_4. After 2 μm deposition of silicon oxide using plasma enhanced chemical vapor deposition (PECVD), we dry oxidize the sample for 3 hours and then anneal in nitrogen atmosphere for 3 hours at 1200°C, in order to increase the oxide quality and drive out residual hydrogen from the PECVD oxide. We measure a record Q of 1.0×10^6 of this device at λ_0=2.6 μm. This is the highest Q reported in this wavelength range.

4.6 Comb Generation

We generate a frequency comb by pumping a cavity resonance of a Si_3N_4microring resonator with a tunable optical parametric oscillator (OPO) source based on periodically poled lithium niobate (PPLN). We use a half-wave plate to adjust input polarization and a lens to focus the pump beam onto the nanotaper coupler of the Si_3N_4 bus waveguide. The light then couples into a ring resonator of radius 230 μm and cross section of 950 nm tall by 2700 nm wide. We collect the output with a lens and measure the comb spectrum with a Fourier transform infrared spectrometer (FTIR), while monitoring a portion of the output on an InGaAs photodiode. To increase the circulating power in the resonator, we tune the pump wavelength into resonance, which causes parametric oscillation and cascaded FWM to occur, resulting in comb generation.

We experimentally demonstrate a frequency comb spanning 2.3 to 3.5 μm, shown in Figure 4.4a, which represents the broadest frequency comb in the MIR demonstrated in a passive microresonator platform. This comb has a free spectral range (FSR) of 99 GHz, and it is generated with a 2.6 μm pump. The pump

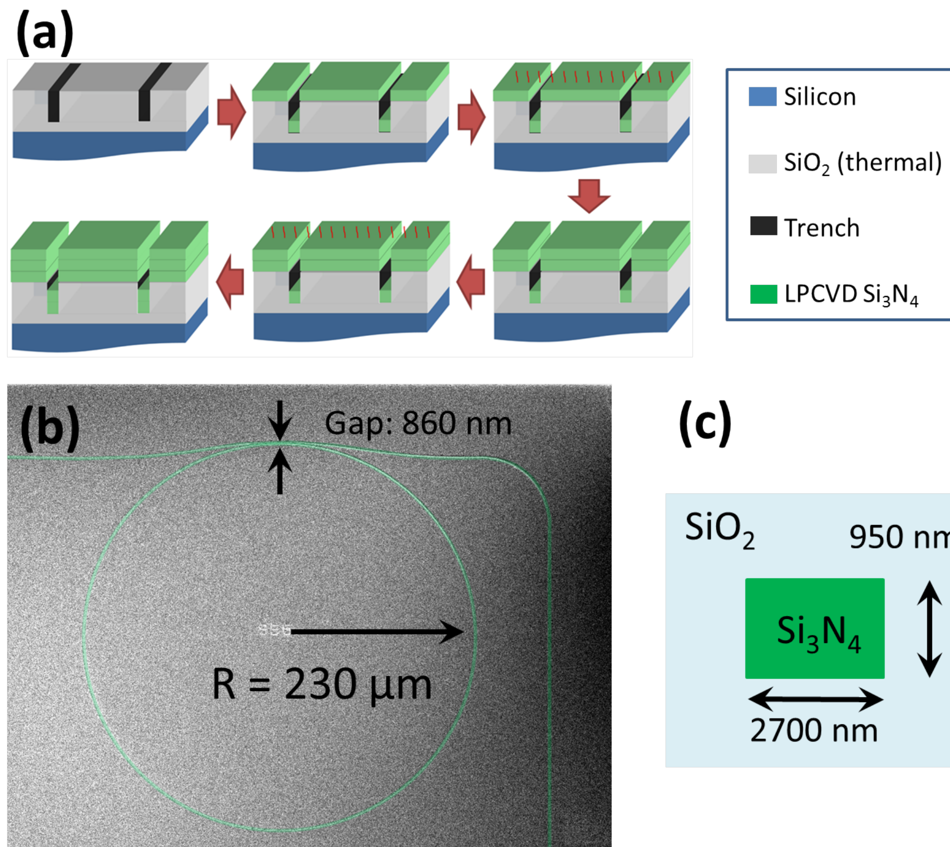

Figure 4.3: (a) Schematic of the deposition-anneal cycling process. After the thermal oxide under-cladding and trenches are formed, we deposit silicon nitride via LPCVD and then anneal at 1200°C. We deposit another silicon nitride layer, anneal, and then deposit the final layer. The final layer is annealed before cladding the devices. (b) Scanning electron microscope image of fabricated ring resonator of radius 230 µm and gap of 860 nm. We implement an adiabatic coupling region as in [2] to minimize excitation of higher order modes. (c) Schematic of resonator cross section of 950 nm tall by 2.7 m wide.

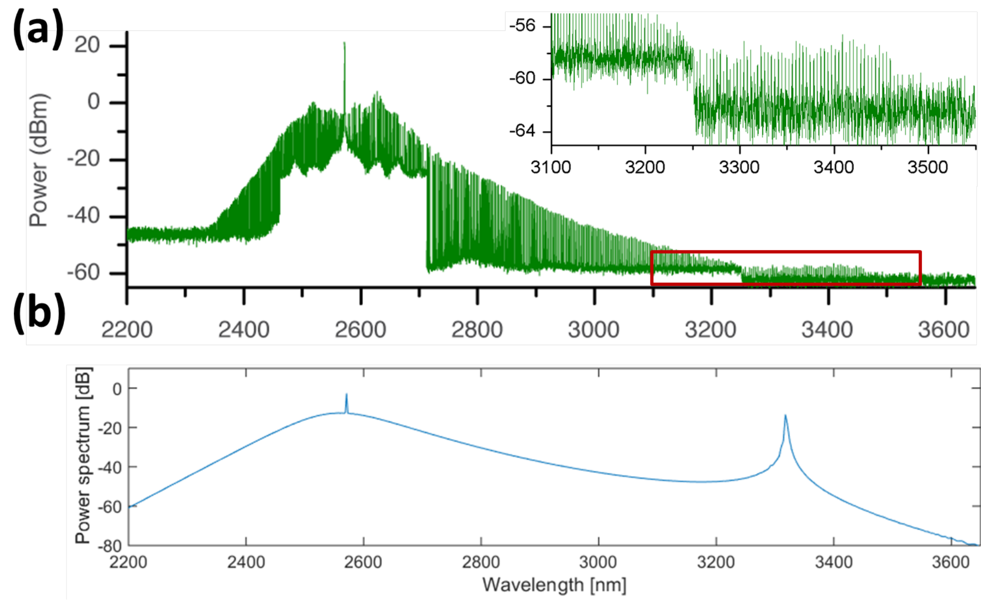

Figure 4.4: (a) Experimentally generated frequency comb spanning 2.3 to 3.5 μm. The different noise floors are due to optical filtering necessary to overcome the limited dynamic range of the FTIR. Inset shows the the dispersive wave beginning to form, as predicted by simulations in (b).

power for the generated comb is 500 mW, and we measure the threshold power to be 80 mW. The resonator has an intrinsic quality factor (Q) of 1.0×10^6 and an extinction ratio of 95% at the pump wavelength. Preliminary RF amplitude noise measurements indicate that the comb is not phase locked, however, based on numerical modeling using the Lugiato-Lefever model [38] (Figure 4.4b), we expect to achieve modelocking with higher power or with higher Q. The Q may be improved with optimized etching and with thinner Si_3N_4deposition-anneal cycling.

4.7 Summary

We have experimentally demonstrated the broadest frequency comb in the MIR generated in a passive microresonator platform. Using thinner deposition-anneal cycling and crack isolation trenches, we overcome material loss and dispersion limitations that have prevented MIR comb generation in Si_3N_4. This work provides a new platform for spectroscopy and gas sensing in the MIR wavelength range.

CHAPTER 5

FREQUENCY COMB GENERATION NEAR VISIBLE WAVELENGTHS

5.1 Introduction

Microresonator-based parametric frequency combs are of interest for their applications to precision frequency metrology, optical clocks, spectroscopy, and biomedical imaging [14, 39]. Comb generation near the visible wavelength range is of particular interest because there are several atomic absorption lines such as the rubidium and cesium lines. Frequency combs can be locked to these lines, providing stable frequency references for frequency metrology and optical clockwork. In addition, the 800 to 900 nm range is of interest for biological applications since it is a suitable compromise between increased scattering loss at shorter wavelengths and increased water absorption at longer wavelengths. The high coherence of frequency comb lines also allows for deeper tissue penetration and higher resolution imaging, particularly for optical coherence tomography [39, 40]. [1]

Previous attempts at broadband comb generation near the visible wavelength range have resulted in combs that are either narrowband or fall below the detection noise floor well before approaching visible wavelengths. For example, comb demonstration was able to overcome this limitation by taking advantage of higher order modes [42], but the generated comb was limited in bandwidth to less than 2 nm. Broadband combs over an octave in spectral width have been generated [43, 25], their spectra remains far from the visible regime. Comb generation closer to the visible wavelength range has been demonstrated by

[1] Portions of this chapter are reproduced from [41]

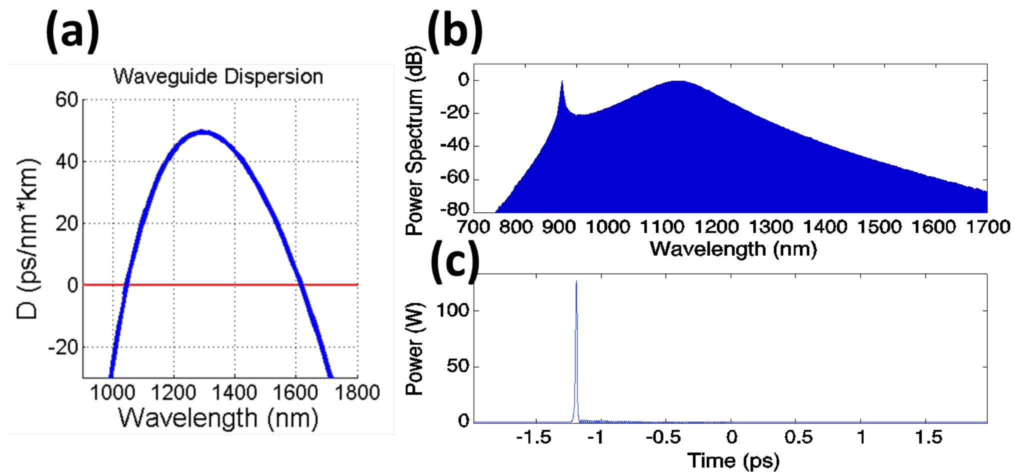

Figure 5.1: Simulations of (a) resonator dispersion, (b) frequency domain of the comb, and (c) time domain of the comb. At high enough pump power or quality factor, we expect to see single-pulse modelocking occur in the resonator.

pumping at 1 μm [44], but the shortest wavelength to which this comb could generate was 950 nm. These combs fail to extend to shorter wavelengths since the group velocity dispersion (GVD) of these microresonator designs cannot adequately compensate for the stronger material dispersion at shorter wavelengths. Anomalous GVD is required for the four wave mixing (FWM) gain that produces parametric oscillation, but the increasingly strong normal GVD of the material as the wavelength approaches the absorption band edge is fundamental to most optically transparent materials.

5.2 Dispersion and Comb Simulation

We engineer the dispersion of a Si_3N_4 ring resonator to overcome the stronger material dispersion at lower wavelengths, and we simulate the comb formation dynamics to ensure broadband comb generation (see Figure 5.1). We use

anomalous waveguide dispersion due to the high confinement of the optical mode to adequately compensate for the normal material GVD of Si_3N_4. While previous demonstrations have also used this approach, we further optimize the dispersion of the ring resonators by simulating the comb formation dynamics for various cross sectional shapes. We simulate the comb spectrum (see Figure 5.1a) using the Lugiato-Lefever model including contributions from higher-order dispersion and self-steepening [38]. The microresonator has a radius of 46 μm and is pumped at 1060 nm with 1.5 W in the coupling waveguide. Our simulations indicate that the comb output exhibits stable, single-pulse mode-locking behavior. Modelocking gives precisely uniform comb spacing, which is desirable for many of the metrology and clocking applications of frequency combs.

5.3 Initial Experimental Comb

Experimentally we generate a frequency comb by pumping a cavity resonance of a Si_3N_4microring resonator with a single-frequency tunable diode laser amplified by a ytterbium-doped fiber amplifier (YDFA). A schematic of the experimental setup is shown in Figure 5.2. We use a polarizing beam cube and a half-wave plate to set the input polarization to quasi-transverse electric (TE) and a bandpass filter to reduce the amplified spontaneous emission (ASE) noise of the amplifier. In order to couple light into the chip, we focus the beam onto the nanotaper coupler of the Si_3N_4 coupling waveguide. The light then couples into a ring resonator with cross section of 690 nm tall by 1400 nm wide, coupling gap of 380 nm, and ring radius of 46 μm (see Figure 5.3). Details of the ring resonator fabrication can be found in [20]. We collect the output with lensed fiber

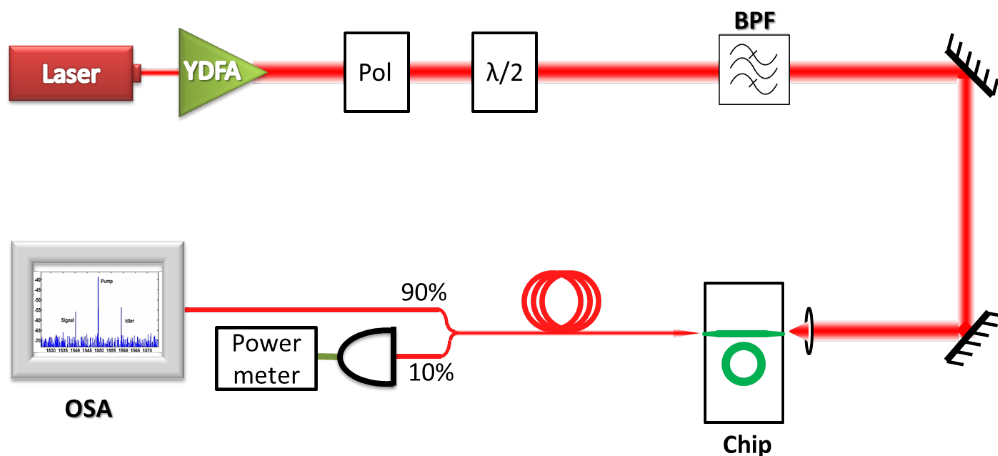

Figure 5.2: Schematic of experimental setup. The broad red beam denotes free-space optics, whereas the narrow red lines denote fiber. YDFA: ytterbium-doped fiber amplifier, Pol: polarizer, $\lambda/2$: half waveplate, BPF: 10 nm bandpass filter centered at 1064 nm, PD: photodiode, OSA: optical spectrum analyzer.

and record the frequency comb spectrum on an optical spectrum analyzer while monitoring 10% of the output power on a detector. To increase the circulating power in the resonator, we tune the pump wavelength into resonance, which causes parametric oscillation and cascaded FWM to occur, resulting in comb generation.

We experimentally demonstrate a broadband frequency comb spanning 830 to 1540 nm, shown in Figure 5.4, which represents, to our knowledge, the broadest comb demonstrated near the visible wavelength range. This wavelength range includes both the D1 and D2 atomic absorption lines of cesium at 895 nm and 852 nm, respectively, to which the frequency comb can be locked. This frequency comb also encompasses much of the range desired for OCT and other biological imaging applications. The demonstrated comb is generated with an amplifier power of 7 W, but this power can be drastically reduced with improved coupling efficiency and quality factor (Q). For the device demonstrated,

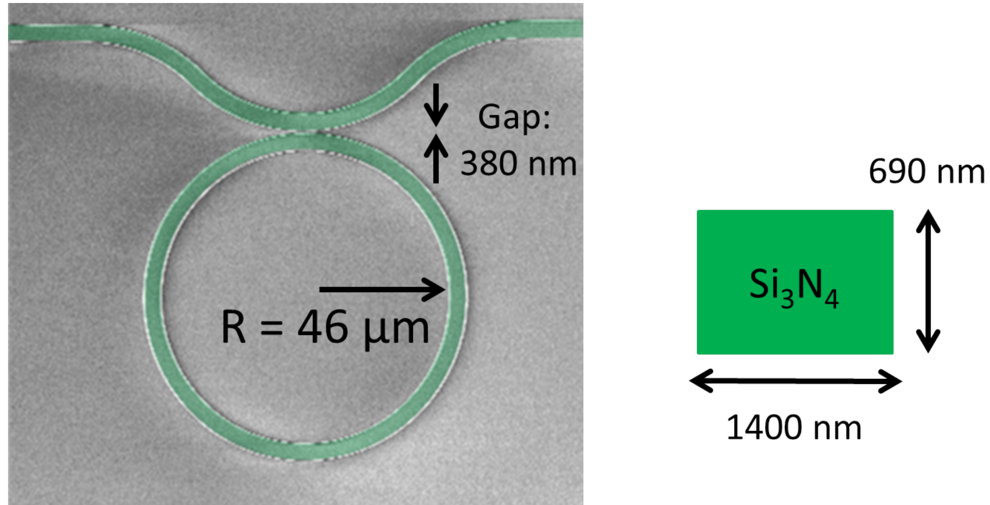

Figure 5.3: (a) SEM of 46 µm ring resonator used to generate frequency comb. Coupling gap is 380 nm, and the ring resonator cross section (b) is 690 nm tall by 1400 nm wide.

we measure a coupling efficiency of 6dB into the chip and loaded Q of 200,000 (intrinsic Q of 700,000), both of which can be further improved. The Q is lower than expected due to resist polymerization issues during fabrication. Since the optical parametric oscillation threshold is inversely proportional to the square of the Q, an increase in Q will dramatically reduce the required amplifier power. These improvements will lower the required amplifier power and increase the bandwidth of the comb. Although we have not yet seen evidence of single-pulse modelocking behavior, simulations confirm that this can occur at higher powers or with the fabrication improvements mentioned above.

5.4 Low Phase Noise Comb

Low phase noise combs are desirable for many applications, in particular optical clocks and precise frequency metrology. However, not all combs exhibit low-

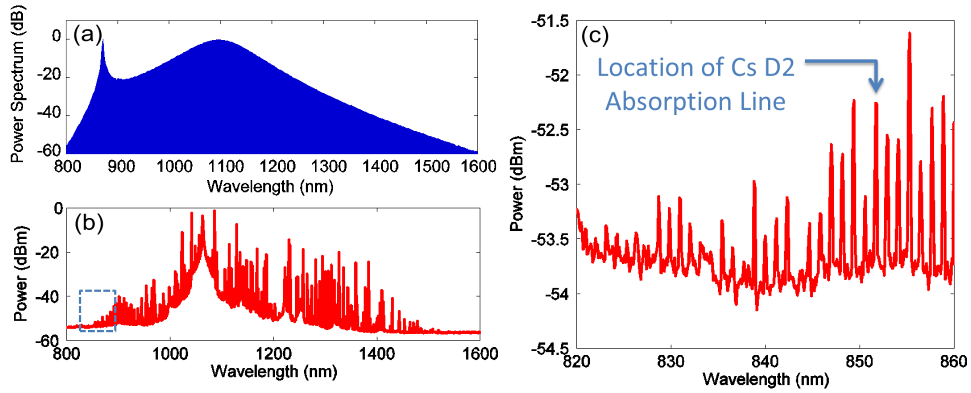

Figure 5.4: (a) Frequency comb simulation , (b) experimentally measured comb, and (c) inset of the comb lines generated at the short wavelength edge of the comb. The predicted comb bandwidth agrees well with that of the measured comb.

noise behavior. Although low-phase noise combs [45, 46, 47] and even mode-locked combs [48, 49] have been demonstrated in the telecom wavelength range, no low-noise combs have been demonstrated near 1 μm.

Demonstrations of low-noise combs in the telecom wavelength range reveal that the low-noise state of the comb is a sudden transition that is accompanied by a sudden reduction in the radio-frequency (RF) noise of the comb [48, 49]. If the low-noise state is attributed to soliton formation within the resonator, we also expect to observe a series of discrete steps in the resonance spectrum while scanning through resonance [49]. These steps correspond to state transitions in which the number of solitons precessing in the cavity decreases with each step. Although these observations of RF reduction and steps in the resonance scan are not necessarily definitive proof of mode-locking, they are consistent with observations of low-noise combs.

We investigate the noise properties of the comb by simultaneously monitoring the pump power in resonance, the total comb power generated, the optical

spectrum of the comb, and the RF noise spectrum of the comb. A schematic of the experimental setup is shown in Figure 5.5. When measuring the combs generated in the other Sections in this chapter (5.3 and 5.5), we see an increase in the low frequency RF noise as we tune the pump into resonance. However, we do not see a characteristic sudden reduction in RF noise as we tune through resonance, which indicates that the comb has not transitioned to a low-noise state. The reason for this is currently still under inverstigation in the scientific community, but this may be due to insufficient resonator enhancement or pump power, improper pump detuning from resonance, undesired dispersion distortion due to mode-couplings, or dispersion in the ring-waveguide coupling itself (see Section 5.7).

We investigate a comb that shows signs of low phase noise. This comb is generated on the same chip as the smooth comb shown in Section 5.5, but with a smaller ring-waveguide coupling gap of 140 nm. While slowly tuning the pump laser through resonance, we separately monitor the output pump power and comb power (see Figure 5.5). We observe the characteristic step signature of a low-noise transition, and then record the optical and electrical spectra before and after the step (see Figure 5.6). On the OSA, we observe a sudden and distinctive change in the state of the comb. The comb before the step has an envelope dominated by a few strong lines, whereas the comb after the step has a more uniform distribution of power throughout the comb. The comb spectra still contains significant power fluctuations, suggesting that the comb is not in a single-pulse state. The RF spectra shows an initially high-noise state, and then a sudden transition to a low-noise state. The observations of a resonance transmission step, sudden state change of the optical spectrum, and sudden drop in the RF noise are consistent with previous observations of low phase-noise

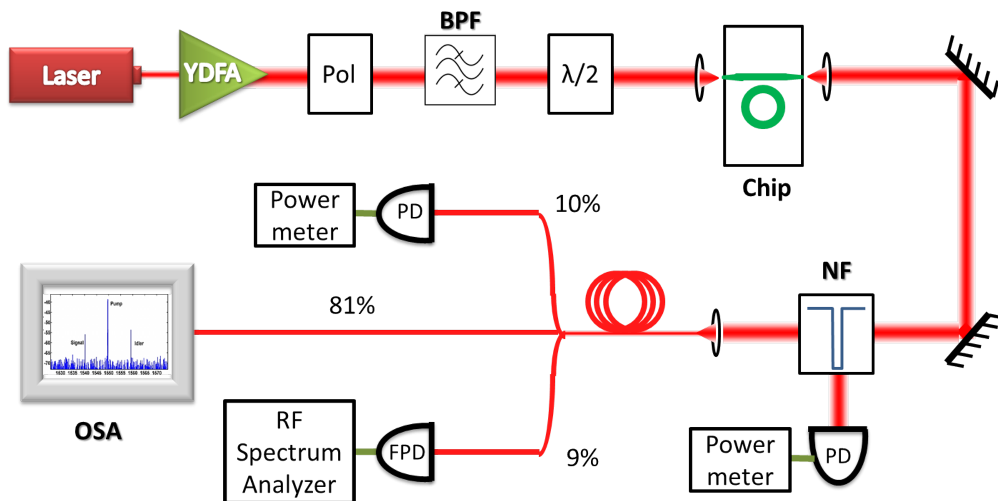

Figure 5.5: Schematic of experimental setup. The broad red beam denotes free-space optics, whereas the narrow red lines denote fiber. The NF allows for monitoring of the reflected pump power and also increases the dynamic range of the OSA. With fiber splitters, we can also simultaneously monitor (not including the pump) the comb power, the optical spectrum, and the electrical noise spectrum. YDFA: ytterbium-doped fiber amplifier, Pol: polarizer, BPF: 10 nm bandpass filter centered at 1064 nm, $\lambda/2$: half waveplate, NF: 50 nm notch filter centered at 1064 nm, PD: photodiode, FPD: fast photodiode (maximum bandwidth of 350 MHz), OSA: optical spectrum analyzer.

combs.

5.5 Smooth Envelope Comb

The comb generated previously in Section 5.3 was an excellent first demonstration of a comb near visible wavelengths, but the comb suffers from strongly varying power levels across the entire spectrum, even among neighboring comb lines (Figure 5.4). However, for many applications, OCT being an example, we desire a comb with slowly varying power levels, ideally across the entire comb

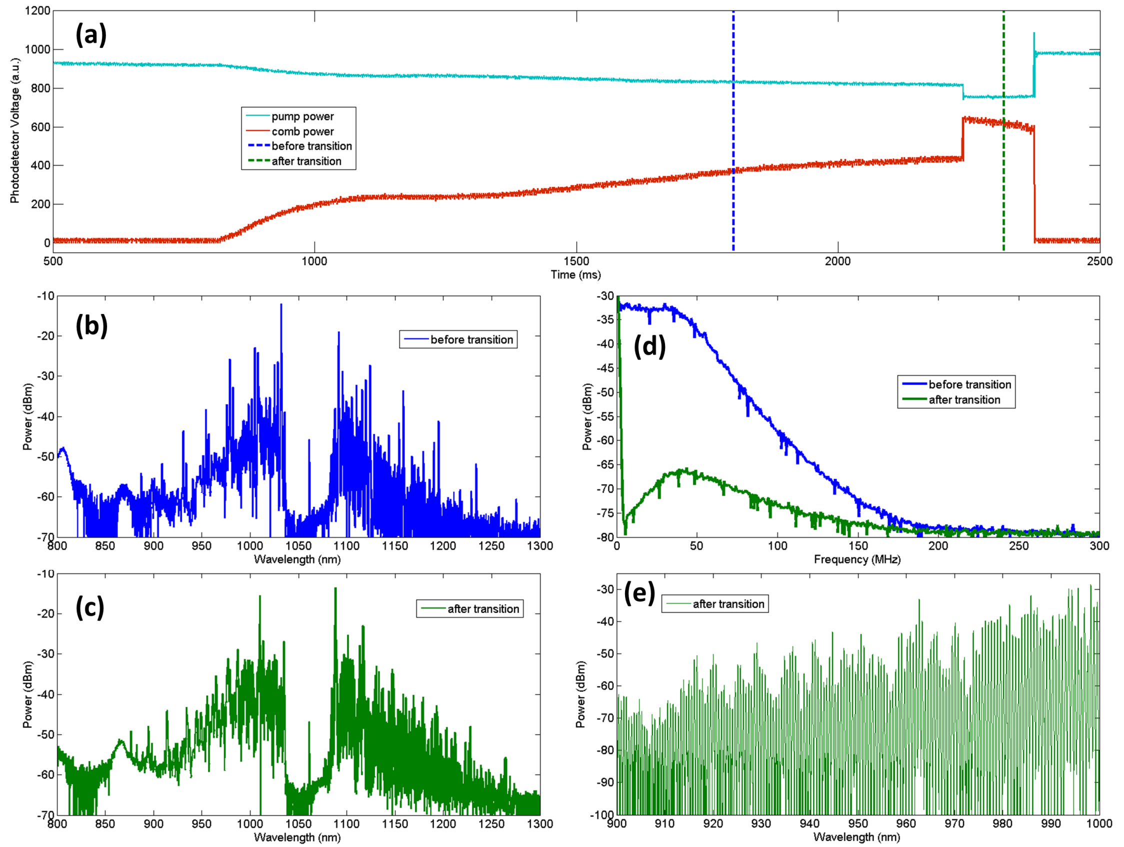

Figure 5.6: (a) Oscilloscope traces of pump power (teal) and comb power (red) while tuning the pump wavelength through resonance. Note the sudden step transition for both pump power and comb power near the end of the scan. This step in the resonance scan is consistent with previous observations of low-noise combs. Measuring the optical spectrum before (b) and after (c) this step reveals a change in the comb structure, also consistent with a comb state change seen in previous observations. We also monitor the comb on a fast photodiode and record the RF noise spectra (d) before and after this transition. The observed drop in the RF noise is also consistent with low-noise observations. The optical spectrum in (e) is an high resolution scan of the comb after the transition, and we verify that the comb remains fully filled in after the transition.

spectrum but at least among neighboring comb lines. Therefore, we seek to generate a comb with a smooth envelope.

The irregular comb envelope from the previous demonstration most likely suffered because of non-optimal dispersion and low Q. While depositing the Si_3N_4 film for the previous set of devices, we were unable to achieve the ideal film thickness of 730 nm because of an unusually low deposition rate of the LPCVD furnace. Therefore, we adjusted the waveguide width to compensate for the thinner film thickness of 690 nm. However, this 40 nm difference in film thickness can have a subtle but significant effect on frequency comb generation, particularly at shorter wavelengths because 40 nm becomes an increasing fraction of the wavelength. The slightly different cross section has a different dispersion than the optimal design, which influences the comb generation process.

Mode-coupling within the resonator is another effect that may have contributed to the irregular power distribution of the comb. This can include coupling between polarization modes, higher-order modes, or combinations of either. The coupling of two modes shifts the refractive index of each mode slightly, which corresponds to a modification of the dispersion of the mode. Depending on the strength of the mode-coupling, these dispersion modification can be strong enough to modify the phase matching conditions around the wavelength where the modes couple most strongly to each other (the wavelength of the "avoided crossing" point). This can then change the distribution of power among comb lines around the crossing point. This distortion in the comb power distribution has been shown in [50] for polarization crossings, but this concept can also be extended to higher-order mode crossings.

The previous comb demonstration also suffered from high insertion and insufficiently high Q, which greatly increased the required input power. The previous comb was generated with 7 W at the input, the maximum output power of the YDFA. However, because of the 6 dB coupling loss per facet, only 1.75 W was accessible to the device itself. This high insertion loss may have also contributed to instability in the experimental setup, which made routine high power experiments challenging. Setup instability makes it very difficult to tune the pump laser into resonance in a repeatable way, and once the comb has been generated, setup instability can randomly transition the comb between different states. Setup instability can also shift the resonance beyond the soft thermal lock, which immediately stops the comb generation process. If we can improve the quality factor of the device, we can significantly lower the power required, as P_{th} is inversely proportional to Q^2 (Equation 1.1).

We use an optimized etch process (see Section 2.4) to reduce mode-coupling within the resonator and to improve the insertion loss and Q. The optimized etch process creates very smooth and vertical sidewalls. This results in waveguides with cross sections that are closer to rectangular, as opposed to trapezoidal because of unintended sidewall angle. A more rectangular cross section reduces the coupling between polarizations and between higher-order modes. Angled sidewalls distort the optical mode of a rectangular waveguide in a way that increases their field overlap with other modes of the structure. As these modes propagate within the ring, they can couple to each other, which distorts the local dispersion, as mentioned above. Therefore, by reducing sidewall angle with the optimized etch, we can reduce the coupling among waveguide modes. In addition, the smooth sidewalls created by this etch also reduce the amount of scattering loss within the resonator, which results in an increase in Q. Finally,

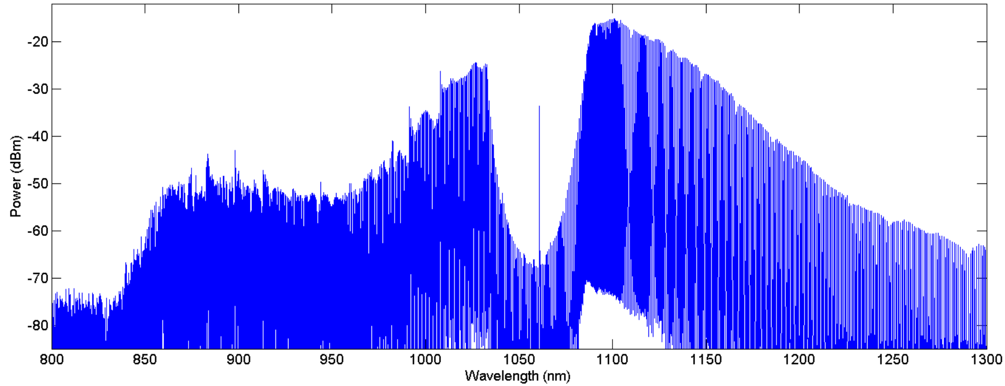

Figure 5.7: Experimentally generated frequency comb with smooth comb envelope. The region around the 1060 nm pump is filtered by a notch filter in order to increase the dynamic range of the OSA. Note the smoother spectrum, particularly around the 850 nm range, which is suitable for OCT applications.

because the optimized etch requires thinner e-Beam resist and has insignificant sidewall angle, we can resolve smaller features, which allows for smaller nanotaper couplers. The improved process (see Section 2.3) could resolve nanotapers between 200-250 nm in width and also severely distorted the sidewalls of the nanotaper. This was the main cause of the high 6 dB per facet coupling loss in Section 5.3, because the optical mode of the nanotaper is smaller and thus mismatched to the mode of the input beam. However, because of the high resolution of the optimized etch, we can resolve extremely small tapers. In fact, because this process also overdevelops the e-Beam resist, the nanotapers also reduce in height gradually, which results in even smaller nanotapers. We improve the coupling loss to 4.7 dB per facet for the device used to generate the comb in Figure 5.7. The overdeveloping of the e-Beam resist may have actually resulted in tapers that are too small, in which case this coupling efficiency can be improved further. At telecom wavelengths we have achieved less than 1 dB per facet with the optimized etch process.

We generate a comb with a smooth envelope (Figure 5.7) by pumping a cavity resonance of the ring resonator. The ring resonator is of radius 115 μm, with cross section 730 nm tall by 1300 nm wide and ring-waveguide coupling gap of 180 nm. The ring is critically coupled, with intrinsic Q of 1.3 million. The comb shown is pumped with 750 mW of power at 1060 nm wavelength. Because of the improvement in the Q and the insertion loss, we suffer less from experimental setup instability.

5.6 Optical Coherence Tomography (OCT) Measurement

We seek to apply a frequency comb for optical coherence tomography (OCT). As mentioned in the Introduction to this chapter, optical frequency combs would provide an excellent light source for high resolution and high depth biological imaging using OCT [39, 40].

A major advantage of an OCT system using a comb source is that it can potentially be extremely compact. Both the comb source and the spectrometer are demonstrated in integrated CMOS-compatible platforms, so they can be in principle combined into a single monolithic device. In addition, for a comb source the path lengths of the reference arm and sample arm of the OCT setup (schematic shown in Figure 5.9) can be extremely unbalanced. This is not the case when using the traditional spectrally filtered source, in which the arm lengths must be matched exactly. This is because depth information is extracted from the interference fringes that are overlayed on the spectrum of the source. The periodicity of these fringes ("fringe spacing") depends on the path length difference (ΔL) between the reference arm and sample arm. When the

path lengths are equal, no fringes appear because $\Delta L = 0$ and the fringe spacing is infinite. As ΔL increases, the fringe spacing decreases. For the traditional source, when ΔL becomes too large and the fringe spacing becomes too small, the signal becomes too weak for detection; much of the source light lies within fringe nodes. The fringe spacing may also become smaller than the linewidth of the source and spectrometer. These limitations constrain the path lengths of the two arms to be close to identical.

However, for a comb source the path lengths can be extremely different. Because comb lines have a much narrower frequency linewidth than the fringe linewidth (even for a ΔL of several meters), less of the source light is "lost" within fringe nodes. In addition, with a comb source, the resolution of the OCT measurement is limited by the comb spacing rather than the spectrometer resolution, because the comb lines are in most cases much narrower in linewidth than the fringe linewidth and the spectrometer linewidth. Because the measurement relies on sampling the interference spectrum, the narrow linewidth of the comb line enables fine detection of changes in the fringe pattern, even if the fringes are very closely spaced (corresponding to large ΔL). Note that for large ΔL we are not actually sampling the exact structure of interference fringes; we are sampling the changing interference pattern, and the way we are sampling gives an identical measurement to the cases of small ΔL. The following example clarifies this further.

For example, if the comb spacing is three times the fringe spacing, each comb line overlaps every third fringe. However, when measuring the interference spectrum on the spectrometer, we observe a spectrum exactly identical to the case of infinite fringe spacing ($\Delta L = 0$), i.e. full transmission of all comb lines. As

ΔL is varied, each comb line experiences interference in the same way it would in the case of small ΔL. This continues as ΔL is increased, until ΔL increases to the point where the comb spacing is now four times the fringe spacing, in which we again observe full transmission of all comb lines. Therefore, for the comb source, in the condition that the comb spacing is an integer multiple of the fringe spacing, the obtained OCT image is identical to the case in which $\Delta L = 0$. This suggests that ΔL can be almost any value, because the measured interference will be identical whenever ΔL is changed by a distance of

$$\frac{c}{n_g \cdot FSR_{comb}} \tag{5.1}$$

where c is the speed of light, n_g is the group index of the ring resonator, and FSR_{comb} is the comb spacing in frequency. If the range of ΔL can be varied within this distance, then we can observe the full range of fringe spacing changes, which is the critical component of the OCT measurement. In this case, the reference arm and sample arm are no longer constrained to be identical, and the path lengths can be as compact or long as desired.

However, OCT measurements using an on-chip frequency comb have not been demonstrated because comb generation in the OCT wavelength range has been challenging because the Q decreases strongly with wavelength. However, this issue was overcome in the previous Section. For high OCT imaging depth, we also require a comb with smaller comb line spacing, which enables finer sampling of the optical spectrum. However, this is challenging because a smaller spacing requires a longer path length resonator, which increases the mode volume and, according to Equation 1.1, also increases the pump power required for comb generation. However, for sufficiently high Q, we can compensate for

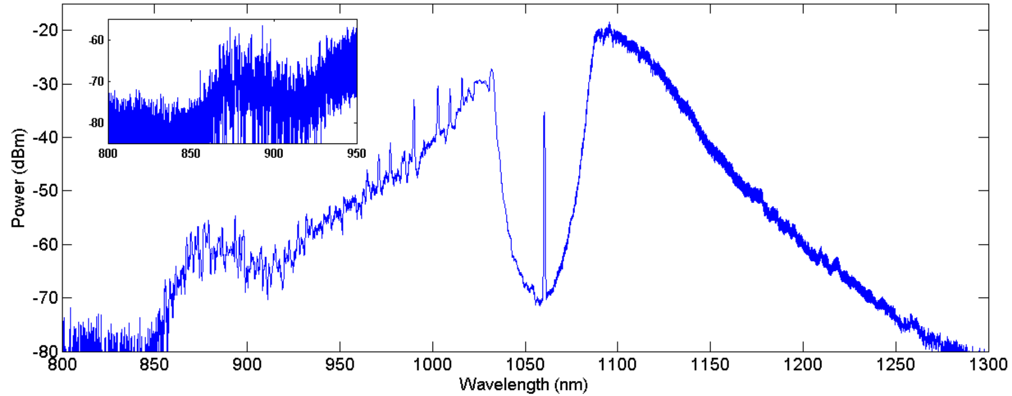

Figure 5.8: Experimentally generated frequency comb with a ring resonator of radius 287 μm, corresponding to 80 GHz comb spacing. The individual comb lines are not resolved because the comb spacing is smaller than the spectrometer resolution. The inset shows a high resolution scan over the range relevant for the OCT measurement. Generation from 800 - 900 nm is ideal, but we successfully obtain images using the generated 850 - 900 nm range.

higher power requirements by increasing the pump power.

We generate a frequency comb (Figure 5.8) as in Section 5.5, but instead we use a ring resonator of radius 287 μm, which corresponds to 80 GHz comb spacing. Because of the finer comb spacing, we cannot generate down to as short a wavelength as in Section 5.5; the larger device radius increases the pump power requirement, and the smaller comb spacing distributes power among more lines within a given comb bandwidth, yielding less power per line. However, the narrower comb bandwidth and lower power per line are sufficient for OCT imaging measurements.

We collaborate with Tornado Spectral Systems (TSS) to perform an OCT measurement on an aspirin pill, using the frequency comb as the light source. TSS developed an on-chip spectrometer, the OCTANE-860, designed specifically for OCT applications. The OCTANE-860 measures 825 - 895 nm with a

dispersion of 0.068 nm/pixel at 860 nm, which corresponds to a pixel spacing of 30 GHz. For OCT measurements, TSS typically uses a superluminescent diode (SLD) with a periodic spectral filter as their measurement source. However, for OCT imaging with our on-chip comb source, we simply replace the traditional spectrally filtered source with our comb source. Although the power of the comb lines in the 850 - 900 nm range is rather low, we can easily compensate for this by increasing the integration time of the OCTANE-860. By varying the reference arm path length, we obtain axial depth information, and by raster scanning the sample, we obtain lateral information. By combining these three degrees of freedom, we generate a full three dimensional image. Using the on-chip frequency comb source with the TSS OCT system, we generate a 3D image of an aspirin pill. Various angles of the 3D image are shown in Figure 5.10. We can clearly distinguish the 'ASPIRIN' text label on the pill. There are a few surfaces that appear above the pill; these are artifacts introduced by non-optimal spectral sampling, and can easily be removed with image post-processing.

We demonstrate the first OCT measurement with a comb source. The use of an integrated light source and spectrometer open up possibilities for fully integrated and portable OCT measurement systems. The additional advantage of tolerance to extreme path length differences between the sample and reference arms can allow compactness that overcomes conventional limitations.

5.7 Pushing Further Towards Visible Combs

Although the combs demonstrated in this section show excellent properties such as flatness and low phase noise, they do not extend into the visible wave-

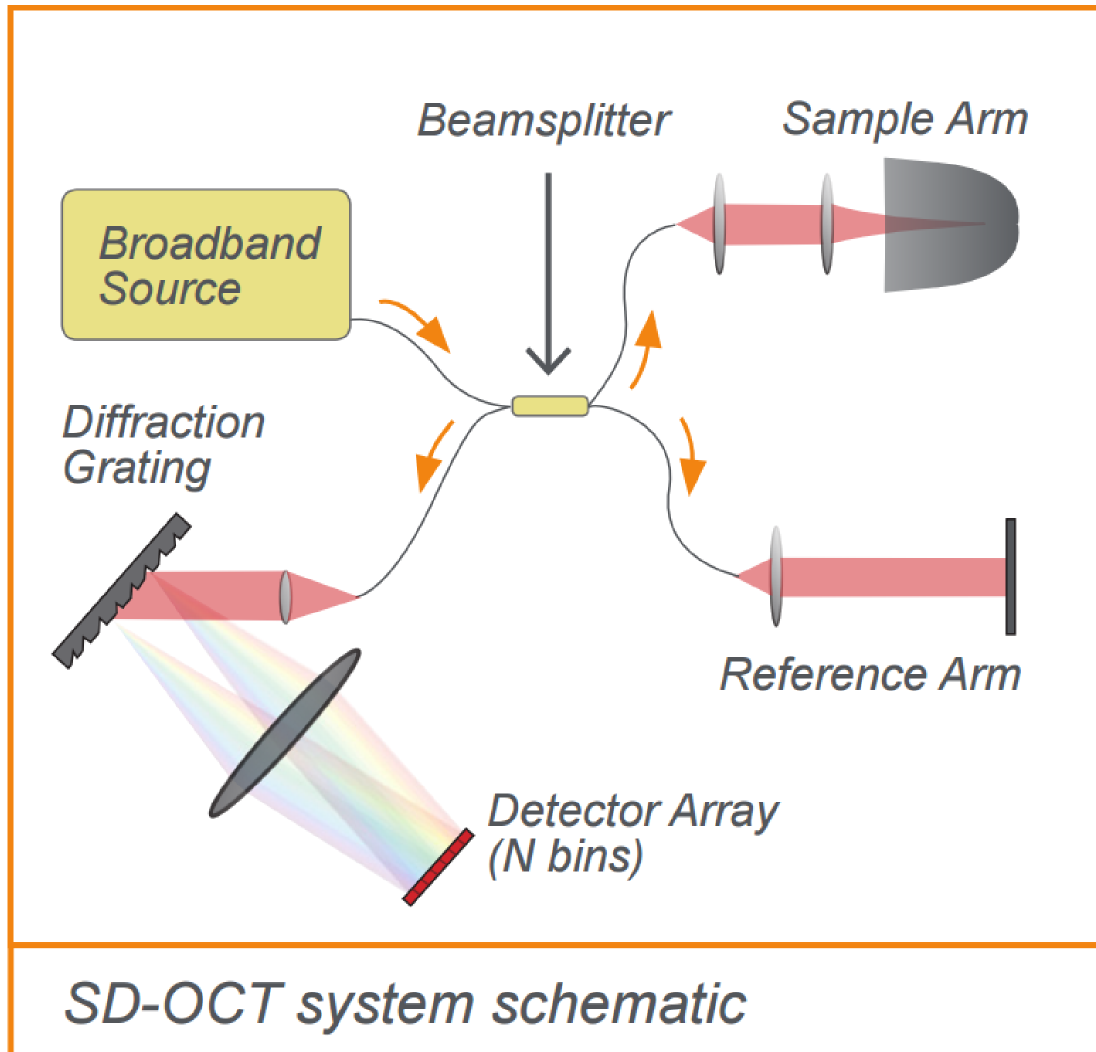

Figure 5.9: Simplified experimental setup for spectral domain optical coherence tomography (SD-OCT). A broadband source is split into a reference arm and sample arm, and then recombined and sent to a spectral detector. By varying the reference arm and analyzing the spectrum, we extract axial depth information. The sample arm is usually raster scanned to obtain lateral information, in order to form a full 3D image. Often, the broadband source is spectrally filtered, but for our measurements we replace the broadband source with a frequency comb source. Image is provided by Tornado Spectral Systems.

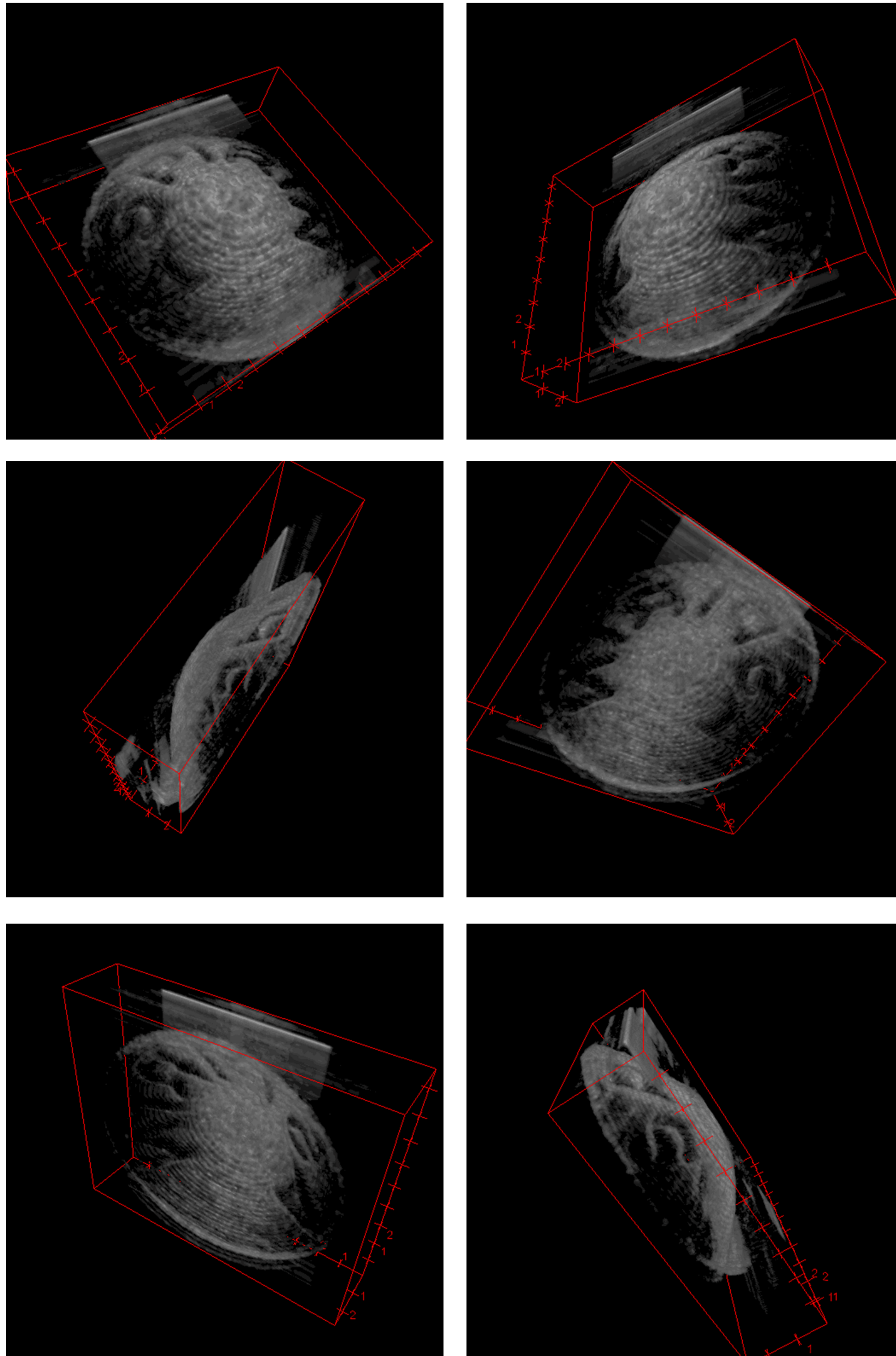

Figure 5.10: Result images of OCT measurement of an aspirin pill using the on-chip frequency comb as the light source. We can clearly distinguish the 'ASPIRIN' text label on the pill. There are a few surfaces that appear above the pill; these are artifacts introduced by non-optimal spectral sampling, and can easily be removed with image post-processing

length range; below 850 nm, comb lines consistently and rapidly decrease in power. One possible contributing factor is the dispersion of the ring-waveguide coupling region. The coupling gap is permanently set during fabrication and is often designed to be in the desired coupling regime (under-coupled, critically-coupled, or over-coupled) for the pump wavelength. However, comb lines far from the pump can experience vastly different coupling conditions because the coupling strength into and out of the ring is a strong function of wavelength. This is a fundamental drawback of any evanescent coupling scheme, because the evanescent field is wavelength dependent. The vast majority of the comb devices that have been demonstrated use some form of evanescent coupling, often via either an integrated ring-waveguide directional coupler or an evanescently coupled pulled fiber.

The dispersion of the coupling region has often been ignored, yet it can be very significant, particularly for short wavelengths and for broadband comb generation. For simplicity, we analyze the wavelength-dependence of a direction coupler (see Figure 5.11). We simulate a directional coupler with two waveguides of cross section 730 nm tall by 1300 nm wide separated by various gaps from 100 nm to 500 nm. We use COMSOL to simulate the optical mode of this structure, and then calculate the total power coupling ratio κ from the splitting of the symmetric and antisymmetric supermodes of the structure. To create a fair comparison, we choose the coupling length of the directional coupler for each gap such that the κ is identical and realistic for critical-coupling in our devices for a pump wavelength of 1060 nm. Although κ is a stronger function of wavelength for larger gaps (mainly because of the longer coupling length), even for the smallest gap of 100 nm, κ decreases by more than a factor of 5 as it approaches 800 nm wavelength.

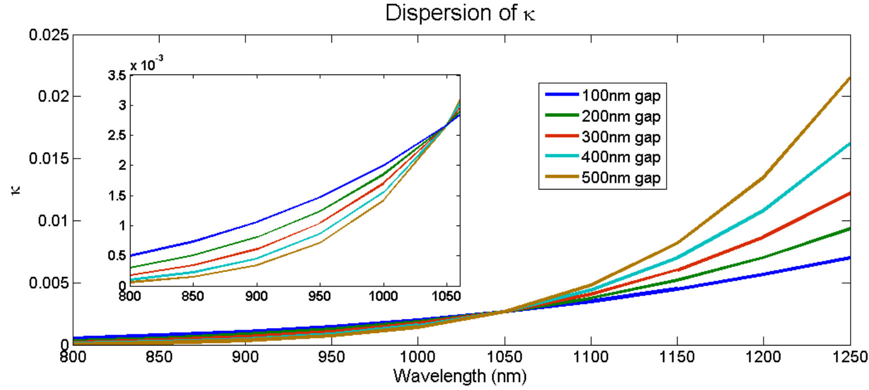

Figure 5.11: Simulation of the coupling strength of a directional coupler across wavelength, for various gaps. For each gap, the coupling length has been adjusted to create identical values of coupling at the pump wavelength of 1060 nm. Note that the coupling is a strong function of wavelength, even for the smallest gap value of 100 nm.

We overcome coupling dispersion by engineering a resonator with a Mach-Zehnder interferometer (MZI) waveguide coupler embedded within the coupling region (Figure 5.12). In order to cancel the dispersive effect of the coupling region, we require an effect that has similar dispersive effect, but with the reversed wavelength dependence. We can achieve this by using an MZI coupler, which has a characteristic periodic spectrum. However, the periodicity of this spectrum is determined by the path length difference (ΔL) of the two arms of the MZI coupler, so we can design this period to cancel the coupling dispersion induced by the directional coupler. Furthermore, we can integrate heaters onto the MZI coupler to dynamically change the coupling strength. These heaters yield the additional ability to finely tune ΔL.

We simulate several ΔL and select the ΔL that can adequately cancel coupling dispersion near the pump wavelength of 1060 nm. The embedded MZI coupling region in the device schematic shown in Figure 5.12 can be considered as a single

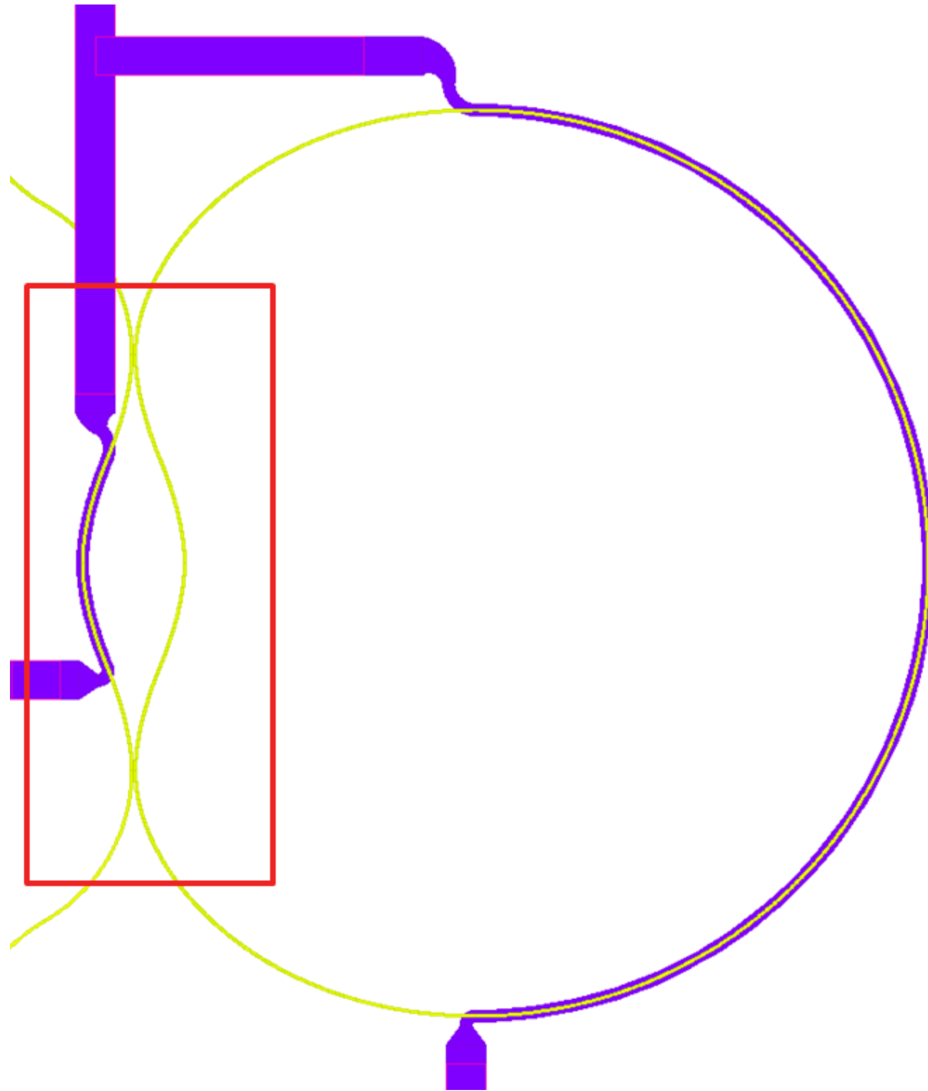

Figure 5.12: CAD of a resonator with MZI coupling region embedded. The heaters (purple) can tune the MZI path length difference (yellow) and the resonator itself (yellow) independently. The area outlined in red can be considered as a single effective coupling region.

coupling region with an effective power coupling ratio of

$$\kappa_{eff} \approx 2\kappa \cos\left(\frac{\pi n \Delta L}{\lambda}\right) \tag{5.2}$$

The refractive index n of the optical mode is also influenced by the temperature change induced by the integrated heater, which is the origin of the heater tunability. The coupling dispersion is contained within the κ term, but the λ term in the cosine expression can potentially compensate for the coupling dispersion. From numerical simulations of Equation 5.2, ΔL of 0.36 μm and 0.5 μm are particularly promising (see Figure 5.13). The former can potentially cancel coupling dispersion at the pump, but also preferentially extracts light at the shorter wavelengths, since κ_{eff} increases strongly. The latter preferentially extracts light at the longer wavelengths, which can be desirable for applications that require light at longer wavelengths, for example 2f-3f referencing using 1030 nm and 1550 nm. Note that these ΔL do not need to be fabricated precisely, because the integrated heaters can tune ΔL continuously.

These devices have been fabricated, and further testing will determine if coupling dispersion is currently the limiting factor for comb generation towards the visible wavelength range.

5.8 Summary

We have experimentally demonstrated broadband frequency comb generation near the visible wavelength range in an integrated Si_3N_4 microring resonator. We have used dispersion engineering and comb dynamics modeling to target

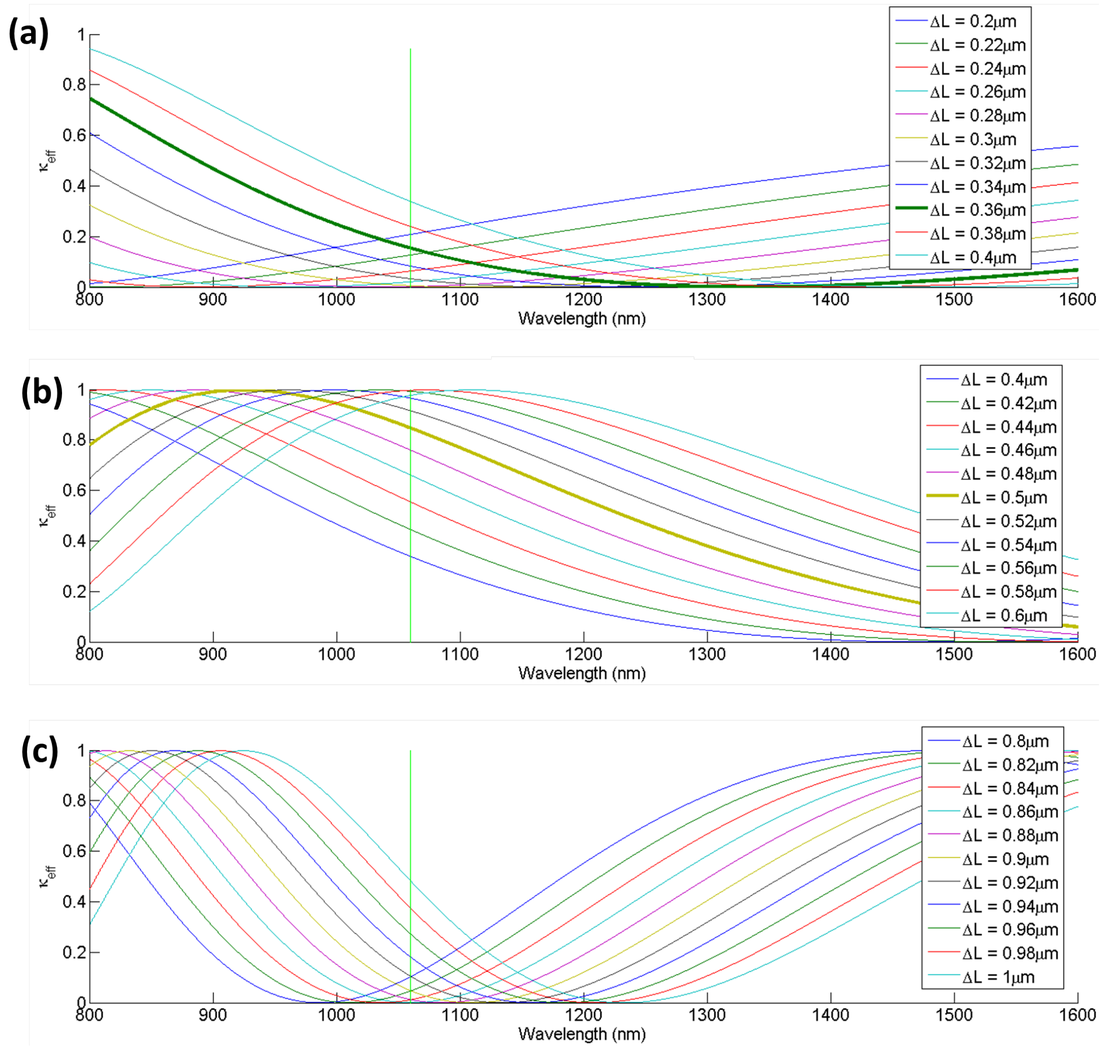

Figure 5.13: Simulation of the embedded MZI coupler for different path length differences using Equation 5.2. In all cases, κ has been set to 0.5, so that the maximum value of κ_{eff} is normalized to 1. For the set of path length differences shown in (a), 0.36 μm (bold green) cancels the coupling dispersion well, and similarly 0.5 μm (bold yellow) in (b). (c) shows that for sufficiently large path length difference, the periodicity changes too quickly; either coupling at the pump wavelength, coupling at the shorter wavelengths, or coupling at the longer wavelengths are significantly blocked.

an optimal geometry for comb generation. We improve upon our initial broadband comb demonstration, and show a smooth envelope comb and a low phase noise comb. We also apply an integrated comb as a source for OCT imaging, acquiring full 3D images. To push further into visible wavelengths, we propose a new design based on a resonator with an embedded MZI. This work provides a platform for integrated advances in frequency metrology, optical clockwork, spectroscopy, and biological imaging.

CHAPTER 6

SUMMARY AND FUTURE WORK

6.1 Higher Q with Thicker Si_3N_4

In the telecom wavelength range, even higher Q may be achievable with thicker Si_3N_4. We have developed a crack isolation trench technique, but we have not yet reached the limit of film thicknesses that can be achieved with this technique. Although the high Q demonstrated in Chapter 3 is beginning to become material limited, the multiple annealing techniques demonstrated in Chapter 4 could be applied to increase the absorption-limited Q. In this case higher confinement due to thicker Si_3N_4 could potentially yield extremely high Q. This is challenging because of the use of double-side polished wafer and film cracking during mid-layer annealing, but it is in principle possible. However, device yield may become a limiting factor.

6.2 MIR Combs with suspended Si_3N_4

The work presented in Chapter 4 was able to demonstrate comb generation up to 3.5 μm, but generation at longer wavelengths is very challenging because of the strong absorption of the silicon oxide cladding. However, this cladding can be foregone altogether. Therefore, air clad structures may be promising for longer wavelength applications. This has an additional advantage of increased refractive index contrast, which may alleviate the need for thick Si_3N_4 films. However, silicon nitride has a strong fundamental absorption peak (the Si—N

bond) near 10 μm, which will ultimately limit how suitable nitride will be far into the MIR. However, the absorption limited Q may still be high enough to work in longer wavelengths.

Air clad Si_3N_4 also has the added advantage of having strong opto-mechanical properties. Si_3N_4 is a commonly used material in opto-mechanics because of its high stress, which can give large mechanical Q's. The mechanical properties may also enable cross-talk of comb lines, which could facilitate a low-noise or mode-locking transition of the comb. This platform offers a new set of rich dynamics to be studied. Air clad Si_3N_4 devices are not necessarily limited to MIR applications, as these dynamics would be interesting to study in any wavelength range.

6.3 Locking to Atomic Lines

A clear follow up to the work presented in Chapter 5 is to apply these combs as optical clocks, stabilizing the combs by directly locking to atomic lines, or carrier-envelope offset stabilization. In this dissertation, we have demonstrated the pieces for this, but for these larger demonstrations, one needs to generate a low-noise comb over sufficient bandwidth. We have shown broadband combs extending to visible wavelengths and low-noise combs on separate devices, but to realize the above applications we must realize these two properties within the same device. However, this should be achievable with high enough Q and accurate comb modeling and dispersion engineering.

6.4 High Resolution OCT Imaging

We presented the first application of combs to OCT imaging in Section 5.6, but the resolution of the images can be greatly improved upon. Many of the limits of the axial resolution and depth penetration were due to non-optimal spectral sampling. However, this can be overcome by matching the comb spacing to the pixel spacing of the spectrometer, and generating comb lines to shorter wavelengths in order to utilize the full spectral window of the spectrometer. This is mostly a technological challenge, which can be overcome by increasing the quality factors of the devices and employing the methods in Section 5.7 to extend the wavelength range of the comb.

BIBLIOGRAPHY

[1] R. W. Boyd, *Nonlinear Optics, Third Edition* (Academic Press, 2008), 3rd ed.

[2] D. T. Spencer, J. F. Bauters, M. J. R. Heck, and J. E. Bowers, "Integrated waveguide coupled Si_3n_4 resonators in the ultrahigh-Q regime," Optica **1**, 153 (2014).

[3] S. Miller, Y. H. D. Lee, J. Cardenas, A. L. Gaeta, and M. Lipson, "Electro-optic effect in silicon nitride," (OSA, 2015), p. SF1G.4.

[4] R. Sun, P. Dong, N.-n. Feng, C.-y. Hong, J. Michel, M. Lipson, and L. Kimerling, "Horizontal single and multiple slot waveguides: optical transmission at = 1550 nm," Optics Express **15**, 17967 (2007).

[5] Q. Li, A. A. Eftekhar, M. Sodagar, Z. Xia, A. H. Atabaki, and A. Adibi, "Vertical integration of high-Q silicon nitride microresonators into silicon-on-insulator platform," Optics Express **21**, 18236 (2013).

[6] M. Zhang, A. Barnard, P. McEuen, and M. Lipson, "Controlling Carbon Nanotube Mechanics with Optical Microcavities," (OSA, 2015), p. FTu4B.8.

[7] M. G. Blain, T. L. Meisenheimer, and J. E. Stevens, "Role of nitrogen in the downstream etching of silicon nitride," Journal of Vacuum Science & Technology A **14**, 2151–2157 (1996).

[8] D. Miller, "Optical interconnects to silicon," IEEE Journal of Selected Topics in Quantum Electronics **6**, 1312–1317 (2000).

[9] M. Haurylau, G. Chen, H. Chen, J. Zhang, N. Nelson, D. Albonesi, E. Friedman, and P. Fauchet, "On-Chip Optical Interconnect Roadmap: Challenges and Critical Directions," IEEE Journal of Selected Topics in Quantum Electronics **12**, 1699–1705 (2006).

[10] R. Soref, "The Past, Present, and Future of Silicon Photonics," IEEE Journal of Selected Topics in Quantum Electronics **12**, 1678–1687 (2006).

[11] T. J. Kippenberg, R. Holzwarth, and S. A. Diddams, "Microresonator-Based Optical Frequency Combs," Science **332**, 555–559 (2011).

[12] A. Gondarenko, J. S. Levy, and M. Lipson, “High confinement micron-scale silicon nitride high Q ring resonator,” Optics Express **17**, 11366–11370 (2009).

[13] P. DelHaye, A. Schliesser, O. Arcizet, T. Wilken, R. Holzwarth, and T. J. Kippenberg, “Optical frequency comb generation from a monolithic microresonator,” Nature **450**, 1214–1217 (2007).

[14] T. Udem, R. Holzwarth, and T. W. Hnsch, “Optical frequency metrology,” Nature **416**, 233–237 (2002).

[15] F. Vollmer, D. Braun, A. Libchaber, M. Khoshsima, I. Teraoka, and S. Arnold, “Protein detection by optical shift of a resonant microcavity,” Applied Physics Letters **80**, 4057–4059 (2002).

[16] S. A. Diddams, L. Hollberg, and V. Mbele, “Molecular fingerprinting with the resolved modes of a femtosecond laser frequency comb,” Nature **445**, 627–630 (2007).

[17] C.-H. Li, A. J. Benedick, P. Fendel, A. G. Glenday, F. X. Krtner, D. F. Phillips, D. Sasselov, A. Szentgyorgyi, and R. L. Walsworth, “A laser frequency comb that enables radial velocity measurements with a precision of 1cms-1,” Nature **452**, 610–612 (2008).

[18] M. Sumetsky, R. S. Windeler, Y. Dulashko, and X. Fan, “Optical liquid ring resonator sensor,” Optics Express **15**, 14376–14381 (2007).

[19] E. Shah Hosseini, S. Yegnanarayanan, A. H. Atabaki, M. Soltani, and A. Adibi, “High quality planar silicon nitride microdisk resonators for integrated photonics in the visible wavelength range,” Optics Express **17**, 14543 (2009).

[20] K. Luke, A. Dutt, C. B. Poitras, and M. Lipson, “Overcoming Si3n4 film stress limitations for high quality factor ring resonators,” Optics Express **21**, 22829–22833 (2013).

[21] M.-C. Tien, J. F. Bauters, M. J. R. Heck, D. T. Spencer, D. J. Blumenthal, and J. E. Bowers, “Ultra-high quality factor planar Si3n4 ring resonators on Si substrates,” Optics Express **19**, 13551–13556 (2011).

[22] K. H. Nam, I. H. Park, and S. H. Ko, “Patterning by controlled cracking,” Nature **485**, 221–224 (2012).

[23] P. Rabiei, W. H. Steier, C. Zhang, and L. R. Dalton, “Polymer micro-ring filters and modulators,” Journal of Lightwave Technology **20**, 1968–1975 (2002).

[24] M. Borselli, T. J. Johnson, and O. Painter, “Accurate measurement of scattering and absorption loss in microphotonic devices,” Optics Letters **32**, 2954–2956 (2007).

[25] Y. Okawachi, K. Saha, J. S. Levy, Y. H. Wen, M. Lipson, and A. L. Gaeta, “Octave-spanning frequency comb generation in a silicon nitride chip,” Optics Letters **36**, 3398–3400 (2011).

[26] H. Jung, R. Stoll, X. Guo, D. Fischer, and H. X. Tang, “Green, red, and IR frequency comb line generation from single IR pump in AlN microring resonator,” Optica **1**, 396–399 (2014).

[27] S.-W. Huang, J. F. McMillan, J. Yang, A. Matsko, H. Zhou, M. Yu, D.-L. Kwong, L. Maleki, and C. W. Wong, “Direct generation of 74-fs mode-locking from on-chip normal dispersion frequency combs,” arXiv:1404.3256 [nlin, physics:physics] (2014). ArXiv: 1404.3256.

[28] A. Schliesser, N. Picqu, and T. W. Hnsch, “Mid-infrared frequency combs,” Nature Photonics **6**, 440–449 (2012).

[29] P. Maddaloni, P. Malara, G. Gagliardi, and P. D. Natale, “Mid-infrared fibre-based optical comb,” New Journal of Physics **8**, 262 (2006).

[30] E. Sorokin, I. T. Sorokina, J. Mandon, G. Guelachvili, and N. Picqu, “Sensitive multiplex spectroscopy in the molecular fingerprint 2.4 m region with a Cr2+:ZnSe femtosecond laser,” Optics express **15**, 16540–16545 (2007).

[31] F. Adler, K. C. Cossel, M. J. Thorpe, I. Hartl, M. E. Fermann, and J. Ye, “Phase-stabilized, 15 W frequency comb at 2848 m,” Optics Letters **34**, 1330 (2009).

[32] A. G. Griffith, R. K. W. Lau, J. Cardenas, Y. Okawachi, A. Mohanty, R. Fain, Y. H. D. Lee, M. Yu, C. T. Phare, C. B. Poitras, A. L. Gaeta, and M. Lipson, “Silicon-chip mid-infrared frequency comb generation,” Nature Communications **6** (2015).

[33] C. Y. Wang, T. Herr, P. DelHaye, A. Schliesser, J. Hofer, R. Holzwarth, T. W. Hnsch, N. Picqu, and T. J. Kippenberg, “Mid-infrared optical frequency

combs at 2.5 m based on crystalline microresonators," Nature Communications **4**, 1345 (2013).

[34] C. Lecaplain, C. Javerzac-Galy, E. Lucas, J. D. Jost, and T. J. Kippenberg, "Quantum cascade laser Kerr frequency comb," arXiv:1506.00626 [physics] (2015). ArXiv: 1506.00626.

[35] A. A. Savchenkov, V. S. Ilchenko, F. Di Teodoro, P. M. Belden, W. T. Lotshaw, A. B. Matsko, and L. Maleki, "Generation of Kerr combs centered at 4.5{\mu}m in crystalline microresonators pumped by quantum cascade lasers," arXiv:1506.00232 [physics] (2015). ArXiv: 1506.00232.

[36] K. Luke, Y. Okawachi, M. R. E. Lamont, A. L. Gaeta, and M. Lipson, "Broadband mid-infrared frequency comb generation in a si3n4 microresonator," Opt. Lett. **40**, 4823–4826 (2015).

[37] M. Borselli, T. J. Johnson, and O. Painter, "Beyond the Rayleigh scattering limit in high-Q silicon microdisks: theory and experiment," Optics Express **13**, 1515 (2005).

[38] M. R. E. Lamont, Y. Okawachi, and A. L. Gaeta, "Route to stabilized ultrabroadband microresonator-based frequency combs," Optics Letters **38**, 3478–3481 (2013).

[39] T. Bajraszewski, M. Wojtkowski, M. Szkulmowski, A. Szkulmowska, R. Huber, and A. Kowalczyk, "Improved spectral optical coherence tomography using optical frequency comb," Optics Express **16**, 4163–4176 (2008).

[40] E. J. Jung, J.-S. Park, M. Y. Jeong, C.-S. Kim, T. J. Eom, B.-A. Yu, S. Gee, J. Lee, and M. K. Kim, "Spectrally-sampled OCT for sensitivity improvement from limited optical power," Optics Express **16**, 17457 (2008).

[41] K. Luke, Y. Okawachi, D. O. Carvalho, M. R. Lamont, A. L. Gaeta, and M. Lipson, "Broadband Microresonator-Based Parametric Frequency Comb near Visible Wavelengths," (OSA, 2014), p. FW1D.3.

[42] A. A. Savchenkov, A. B. Matsko, W. Liang, V. S. Ilchenko, D. Seidel, and L. Maleki, "Kerr combs with selectable central frequency," Nature Photonics **5**, 293–296 (2011).

[43] P. DelHaye, T. Herr, E. Gavartin, M. L. Gorodetsky, R. Holzwarth, and T. J.

Kippenberg, “Octave Spanning Tunable Frequency Comb from a Microresonator,” Physical Review Letters **107**, 063901 (2011).

[44] K. Saha, Y. Okawachi, J. S. Levy, R. K. W. Lau, K. Luke, M. A. Foster, M. Lipson, and A. L. Gaeta, “Broadband parametric frequency comb generation with a 1-m pump source,” Optics Express **20**, 26935–26941 (2012).

[45] S. B. Papp and S. A. Diddams, “Spectral and temporal characterization of a fused-quartz-microresonator optical frequency comb,” Physical Review A **84**, 053833 (2011).

[46] F. Ferdous, H. Miao, D. E. Leaird, K. Srinivasan, J. Wang, L. Chen, L. T. Varghese, and A. M. Weiner, “Spectral line-by-line pulse shaping of on-chip microresonator frequency combs,” Nature Photonics **5**, 770–776 (2011).

[47] P. DelHaye, K. Beha, S. B. Papp, and S. A. Diddams, “Self-Injection Locking and Phase-Locked States in Microresonator-Based Optical Frequency Combs,” Physical Review Letters **112**, 043905 (2014).

[48] K. Saha, Y. Okawachi, B. Shim, J. S. Levy, R. Salem, A. R. Johnson, M. A. Foster, M. R. E. Lamont, M. Lipson, and A. L. Gaeta, “Modelocking and femtosecond pulse generation in chip-based frequency combs,” Optics Express **21**, 1335 (2013).

[49] T. Herr, V. Brasch, J. D. Jost, C. Y. Wang, N. M. Kondratiev, M. L. Gorodetsky, and T. J. Kippenberg, “Temporal solitons in optical microresonators,” Nature Photonics **8**, 145–152 (2014).

[50] S. Ramelow, A. Farsi, S. Clemmen, J. S. Levy, A. R. Johnson, Y. Okawachi, M. R. E. Lamont, M. Lipson, and A. L. Gaeta, “Strong polarization mode coupling in microresonators,” Optics Letters **39**, 5134 (2014).